Plasma-Wave Amplification in Bismuth

D. J. BARTELINK
Bell Telephone Laboratories, Murray Hill, New Jersey 07974
(Received 25 June 1969)

The amplification properties of Bi at 4.2°K with parallel applied current and magnetic field are demonstrated experimentally and compared with theory. The threshold for low-frequency wave propagation requires a minimum critical ratio of current to magnetic field corresponding to a waveguide cutoff independent of frequency. A parameter Δ, based on the average difference of hole- and electron-mobility anisotropy, affects the spatial growth of these waves in direct proportion to $|\Delta|$. For samples oriented to minimize $|\Delta|$, studies of waveguide cutoff show that collision damping in the body of the guide, as expressed by the dielectric tensor derived by Misawa, is sufficient to account for the observed details, and that simple metallic boundary conditions appear to be sufficient to account for the boundary field matching. Crystal orientations for optimum gain (maximum $|\Delta|$), namely, 8° off the Z axis along a $-Y$ direction, exhibit gain in approximate quantitative agreement with theory. Also predicted and observed is an absolute instability oscillation occurring at currents greater than twice waveguide cutoff. In the following, three side effects are also described: (1) a depressing effect on the gain by the azimuthal magnetic field of the current and a curved current-voltage relation resulting from self-magnetoresistance; (2) additional pronounced nonlinearities of the current-voltage relation due to phonon emission when the electron-drift velocity exceeds the lattice-sound velocity, and an accompanying enhancement of amplification by a mechanism that can be made plausible; (3) feedback oscillation exhibiting the properties of the gain mechanism. The maximum frequency for amplification was about 100 kHz. Higher frequency limits have been explored, but only by extrapolation of the theory for Bi, because the high carrier mobilities make that material about the best available.

I. INTRODUCTION

PRELIMINARY results have previously been reported[1] on the observation in Bi at 4.2°K of amplification of a type of transverse waves similar to helicon waves. A detailed theory[2] of the effect in bulk plasmas has also been given with passing reference to the effect of a finite diameter waveguide of the material. We present here (1) detailed experimental observations and their correlation with theory on amplification and absolute instability, (2) the effect of a waveguide in the presence of collision damping, and (3) certain side effects which tend to obscure and sometimes enhance effects within the range of parameters otherwise best suited for the study of amplification. These side effects are (1) the self-magnetic field induced by the static applied current, (2) the emission of phonons when the carrier-drift velocity exceeds the velocity of sound in the lattice, and (3) a feedback oscillation set up by reflections from the end boundaries of the sample.

Experimental observations consist of the voltage response of a pickup coil located near one end of the specimen, as shown in Fig. 1(a), under conditions of zero or constant rf excitation of the coil at the opposite end. These results are most readily presented as an oscilloscope trace wherein the horizontal deflection is proportional to the current through the specimen. Figure 2(a) shows, schematically, a typical example. There are several regions (A–E), which result from the first-order effect of current on wavelength and, in turn, the influence waveguide cutoff on the observable excitation. In abbreviated designation, to be discussed in Sec. II, these regions may be characterized by A, damped Alfvén waves; B, rotation of axis of polarization; C, waveguide cutoff transition; D, free propagation or amplification; and E, absolute instability.

Section II gives a brief interpretation of the ideal model of Ref. 2 in each of these regions. For region C, use is made also of Appendix A, which considers wave propagation at an angle to the static magnetic field. A description of the experimental samples and methods is given in Sec. III.

Section IV presents a correlation of experimental re-

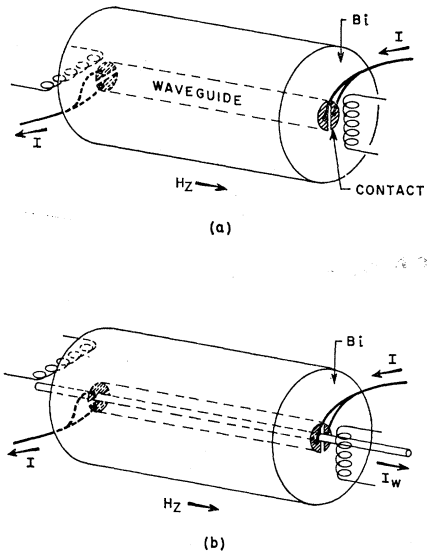

FIG. 1. (a) Schematic view of Bi structure showing waveguide in which wave amplification occurs. (b) Same as (a) except for the addition of a coaxial wire carrying a current I_w for reducing the azimuthal field H_φ.

[1] D. J. Bartelink, Phys. Rev. Letters **16**, 510 (1966).
[2] D. J. Bartelink, Phys. Rev. **158**, 400 (1967).

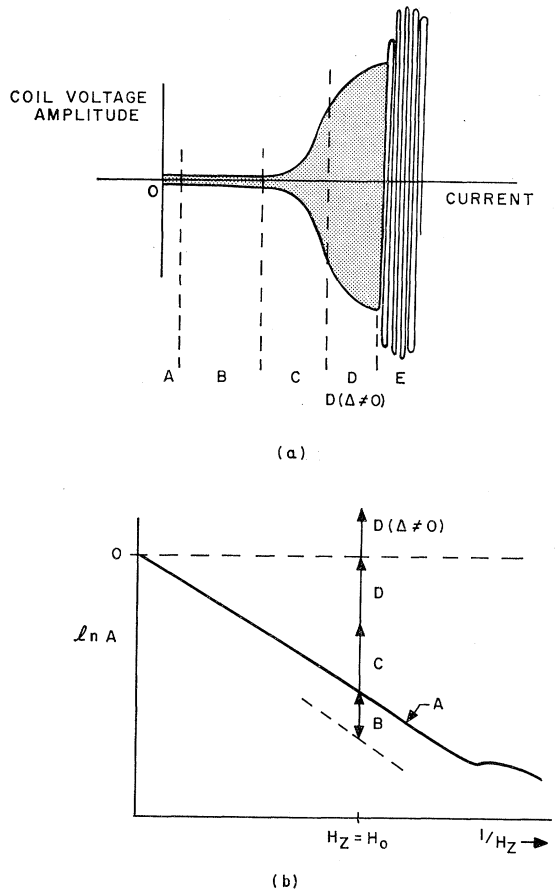

FIG. 2. (a) Schematic representation of a typical experimental amplitude response as a function of current, showing the regions A–E described in the text. (b) Plot of $\ln A$ versus $1/H_z$, which yields a linear relation for damped Alfvén waves (curve A), showing also the relative amplitudes at $H_z=H_0$ for regions A–D.

sults and theory appropriate to regions C and D for a specimen oriented so as to minimize the anisotropy parameter Δ. In Ref. 2, it is shown that for Bi with $\Delta=0$ there will be no amplification and that transmission will be reciprocal. Reciprocity is an optimum condition for investigating cutoff behavior, and the absence of gain prevents the occurrence of feedback oscillation. No special precaution was taken to avoid the other two side effects, although their influence was only moderate. Section IV also gives results on amplification and absolute instability which agree well with theory because the sample used had a configuration suitable for minimizing the azimuthal magnetic field H_φ. For this purpose, a coaxial wire, as shown schematically in Fig. 1(b), was used to carry a current opposing the current in the Bi. A result of its use was that the maximum drift velocity in the sample could be kept smaller than the sound velocity for this measurement. The sample was also constructed to minimize the feedback oscillations by means of a suitable geometry.

Section V deals with sample characteristics which, although not all directly related to plasma waves, illustrate the side effects listed above. They are, thus, essential in the full understanding of the behavior of the samples of Sec. IV. Section VI considers some of the features of amplification based on power dissipation computations presented in Appendix B and gives an interpretation of gain enhancement by phonon emission. A novel gain mechanism for helicon waves in metals with open orbits is also proposed.

II. IDEAL MODEL

In the absence of current (region A), the only waves in the compensated Bi plasma with frequencies less than the collision frequency are damped Alfvén waves. Their properties[3] are a signal decay of $e^{-2\pi}$ per wavelength, while the attenuation per unit length is a function of magnetic field. A plot of $\ln A$, where A is the transmission-amplitude ratio, versus the reciprocal of the magnetic field H_z yields a linear relation for large fields, as has been demonstrated experimentally (see Fig. 4 of Ref. 3) and is shown schematically in Fig. 2(b), curve A. Extrapolation to $H_z=\infty$, where the wavelength becomes infinite gives the value of $\ln A$ for which the wave-transmission loss is zero. In principle, it allows us to determine experimentally the insertion loss for a sample transmitting a lossless wave. Stated differently, we can read from Fig. 2(b) for any value of H_z, independently of the launching and detecting efficiency, the growth in amplitude expected if a damped Alfvén wave were to be transformed into a lossless wave. The values will actually differ by a factor of 2 if both circularly polarized components of damped Alfvén waves were launched, because the propagating wave consists of a single component.

In this experiment, the situation is not clear cut, however, since it has been assumed that equal cross-sectional areas apply to both wave modes while, in fact, they differ [see Fig. 1(a)]. The propagating wave will be confined to a waveguide given by the current beam, while the damped Alfvén waves permeate a larger area. Damped Alfvén waves are linearly polarized, furthermore, and in order to detect a maximum signal, the detector polarization must be adjustable. The polarization is not adjustable in the present experiments, but we have found, nevertheless, an order-of-magnitude agreement on amplitude variation with current.

The effect of drift current on signal amplitude of damped Alfvén waves (region B) is given by Eq. (1) of Ref. 2. For the case of Bi at low frequencies ($\delta n=0$, $\omega^2/V_A^2 \ll kj/H_z$),

$$k_z^2=\pm k_z j/H_z-i\omega en/H\langle\omega_c\tau\rangle. \quad (1)$$

We have added subscript z to wave number k because the results of Ref. 2 apply only for $\mathbf{k}$ directed along the magnetic field $\mathbf{H}$. The parameters in Eq. (1), such as

[3] D. J. Bartelink and W. A. Nordland, Phys. Rev. **152**, 556 (1966).

current density j, and the average of the product of cyclotron frequency and relaxation time over all carrier species $\langle\omega_c\tau\rangle$ are defined in Ref. 2, where the extent of the influence of small $\omega_c\tau$ values is also noted. The second term on the right-hand side in Eq. (1) describes damped Alfvén waves when $j=0$, and the first term leads to a Faraday rotation because it, respectively, adds to and subtracts from the magnitude of the wavenumbers of the two polarization components of the damped Alfvén waves.[4] The amplitude variation induced by this rotation is indicated schematically by arrow "B" in Fig. 2(b).

Damped Alfvén waves pass through a medium with little influence being exerted by the boundaries.[3] As the wave becomes more freely propagating (region C), signals radiated by the source at an angle θ relative to the direct transmission line (our z direction) also contribute to the output and must be taken into account. The resulting waveguide transmission problem divides into two parts: (1) determination, in an infinite medium having the properties of the waveguide material, of the propagation and attenuation characteristics at angle θ relative to the direction of $\mathbf{H}$; (2) the field matching problem at the (usually cylindrical) boundary between the regions with and without current. We do not work out the details of the second part here because most of the observable waveguide effects are due to added damping within the body of the waveguide material. This damping results, in effect, from the extra path length that the wave experiences near cutoff and, although the precise angle θ is important, the detailed field matching is not. The reason is that the waves inside the cylinder, because of the existence of a large net Hall effect, have particularly small ratios of longitudinal electric field to azimuthal magnetic field, unequalled by any waves in the surrounding medium (damped Alfvén waves). It has been found,[5] therefore, that the only suitable field matching involves a "surface wave"[6] which is able to match the fields of the inside wave. Since the surface wave, for all but the smallest values of $\omega_c\tau$, has a very small transverse penetration from the boundary normal metallic waveguide conditions are appropriate. Throughout this paper, therefore, we use, for a cylindrical waveguide of radius r, the lowest-order transverse wave number

$$k_\perp = 2.405/r. \tag{2}$$

In Appendix A, we have made use of the dielectric tensor calculated by Misawa,[7] as it applies to Bi in the limit $\omega\tau \ll 1$, to determine the change in Eq. (1) needed to make it applicable to propagation at an angle to $\mathbf{H}$. The dispersion relation calculated from Eq. (A31) for $\Delta=0$ is

$$k^2 = \pm k\frac{j}{H_z(1+\Theta)} - \frac{i\omega en\gamma}{H_z\langle\omega_c\tau\rangle\cos\theta}, \tag{3}$$

where

$$k^2 = k_z^2 + k_\perp^2; \quad k_\perp/k_z = \tan\theta, \tag{4}$$

$$2\gamma = \cos\theta + (1-\Theta)/\cos\theta, \tag{5}$$

$$\Theta = (\tan^2\theta)/\langle\omega_c\tau\rangle\langle\langle\omega_c\tau\rangle\rangle. \tag{6}$$

Equation (3) is valid, within the limitations consistent with Appendix A and Ref. 2, at magnetic fields for which $\langle\omega_c\tau\rangle \sim 1$ (where $\langle\omega_c\tau\rangle$ is defined in Ref. 2, and $\langle\langle\omega_c\tau\rangle\rangle$ is defined in Appendix A). Θ represents the first-order correction term of the θ dependence at low magnetic fields. When $k\neq 0$, Eq. (3) can be rewritten as

$$k_\pm^2 = \frac{j^2}{H_z^2(1+\Theta)^2} - \frac{i\omega en\gamma}{H_z\langle\omega_c\tau\rangle\cos\theta} \times\left(1\pm\frac{j}{k_\pm H_z(1+\Theta)}\right), \tag{7}$$

where the $\pm$ subscript has been added to k to designate the two polarization solutions. When the imaginary term in Eq. (7) is small compared with the real term, as it will always be for some small ω or large j, the expression in large parenthesis multiplying it approaches the value 2. Using Eqs. (4), (5), and (7), we then solve for θ, neglecting terms of order Θ^2, and obtain

$$k_{z\pm} \simeq \pm\frac{J}{H_z} \mp \frac{i\omega en}{J\langle\omega_c\tau\rangle}\left[1+k_\perp^2\left(\frac{2J^2}{H_z^*} - \frac{2i\omega en}{H_z\langle\omega_c\tau\rangle}\right)^{-1} \times\left(1+\frac{1}{\langle\omega_c\tau\rangle^{3/2}\langle\langle\omega_c\tau\rangle\rangle^{1/2}}\right)\right], \tag{8}$$

where

$$J^2 = j^2/(1+\Theta)^2 - k_\perp^2 H_z^2. \tag{9}$$

It is clear that a cutoff occurs when j is less than the value

$$j_c = k_\perp H_z(1+\Theta). \tag{10}$$

Equation (8) also shows that for j just above j_c, where J is small, the damping is enhanced, and we will use subscript $c0$ to denote the observable signal threshold in accordance with a definition given below.

At current densities well above j_c (region D), the damping reduces with increasing j so that higher-frequency propagation becomes possible. We note that k has no other frequency dependence, so that the nominal wavelength is independent of ω. The polarization characteristics are best obtained from Eq. (3) by dividing by k. Note that opposite polarizations propagate in opposite directions. The alternate polarization in a given direction is the $k\sim 0$ solution discarded in the division by k (see also Ref. 2). It will suffer strong collision damping, as seen from Eq. (7) with $k_\pm \sim 0$, or,

[4] D. J. Bartelink, Phys. Rev. Letters **12**, 479 (1964).
[5] D. J. Bartelink, Bull. Am. Phys. Soc. **10**, 384 (1965).
[6] C. R. Legendy, Phys. Rev. **135**, A1713 (1964); J. P. Klozenberg, B. McNamara, and P. Thonemann, J. Fluid Mech. **21**, 545 (1965); G. A. Baraff and S. J. Buchsbaum, Phys. Rev. **144**, 266 (1966).
[7] T. Misawa, Japan. J. Appl. Phys. **2**, 500 (1963).

in the very weak damping limit, a waveguide cutoff. In contrast, normal helicon waves, given by $kk_z=\pm\omega e\delta n/H_z$ (see Ref. 2), propagate with the same polarization in both directions, and the alternate polarization does not propagate because k_z becomes imaginary.

These freely propagating waves become spatially growing [region D ($\Delta\neq 0$)] when net negative collisional damping results from a nonzero value of the anisotropy parameter Δ (see Ref. 2). The expression analogous to Eq. (8) for $\Delta\neq 0$ can be determined from Eq. (A31). Neglecting the Θ dependence and retaining only lowest order in $k_\perp$, we obtain[8]

$$k_{z\pm}=J/H_z[\pm 1+(i/\langle\omega_c\tau\rangle)(\Delta\mp\omega enH_z/J^2)]. \quad (11)$$

Note that when $\omega\rightarrow 0$ (small inherent damping), gain will occur for very small Δ, i.e., $V_\varphi=\omega/k\rightarrow 0$. The condition giving the maximum frequency at which gain occurs is

$$\omega\leq\omega_{\max}\equiv\Delta J^2/enH_z. \quad (12)$$

Absolute instability (region E) sets in when j exceeds[1,2]

$$j_{th}\simeq 2k_\perp H_z, \quad (13)$$

which is approximately double j_c. The decrease in growth rate at small values of $\langle\omega_c\tau\rangle$, illustrated by Fig. 5 of Ref. 2, and the θ dependence, discussed in Ref. 1 and in connection with the present Eq. (8), make it reasonable to expect that the instability will be suppressed for some range of j exceeding j_{th}. No quantitative formulation of this effect has been made.

III. EXPERIMENTAL SAMPLES AND TECHNIQUES

The experimental samples used in this paper were prepared from single-crystal material grown by a technique of regrowth in supercooled melt. Large-volume crystals were produced using a vibration-free mounting. The crystals had a very low density of small-angle grain boundaries and resistivity ratios between room temperature and 4.2°K of better than 300. Spark machining apparatus was used to obtain the detailed sample shapes. The large electrical contacts were soldered with 40–60 tin-lead solder, while other connections were made with Wood's metal.

Figure 3 shows the various parts used in fabricating three specific samples, B-10, B-14-3, and B-27. All three configurations have the benefit of an integral heat sink and enhanced structural strength, which is of utmost importance in obtaining working samples of Bi. Bi is a fragile material, particularly at 4.2°K. The current carrying portion which can be, and has been, made very thin is embedded in a large structurally strong block to which contacts can be attached without causing damaging strains.

Because of the large transverse magnetoresistance ratio of Bi, the cross-sectional shape and size of the contacts in Fig. 3(b) determine a waveguide shape with a net current carrying area $\mathfrak{A}$, as shown in Fig. 3(a). Ideally the axial alignment of samples B-10 and B-27 is adjusted to be parallel to **H** but the strip contacts of B-14-3 have the property that the waveguide shape of Fig. 1(a) is maintained over a range of angles. This configuration is useful in varying the crystallographic direction while the sample is in operation. (The self-magnetic field of the current may tend to round off the corners on the square waveguide formed in this geometry by its own beam-confining action.) Sample B-27 had a hole in the crystal concentric with the waveguide. A current carrying wire in this hole was used to modify the self-magnetic field. The wire consisted of several strands of fine copper wire.

Aside from the difference in contact shape, samples B-14-3 and B-27 also differed in crystal orientation, corresponding approximately to minimum and maximum values of $|\Delta|$, respectively. The contact axis was directed along orientations relative to the Z axis of 40° along a $+X$ direction and 8° along a $-Y$ direction, respectively. While no detailed calculations have been performed to determine if these are the proper orientations (the relaxation time anisotropy is not that well known), a big difference is observed experimentally. For sample B-27, a value $\Delta=-0.6$ is estimated from the mass parameters of Smith, Hebel, and Buchsbaum[9] and the relaxation times of Zitter.[10]

The over-all diameter of the contacts shown in Fig. 3(b), about 1 cm, exceeded the length of the coils inserted in them [Fig. 3(c)]. The coils were made of a single layer of No. 50 wire wound on large resistance value $\frac{1}{8}$-W resistor bodies and were encapsulated with shrinkable tubing. The end blocks [Fig. 3(c)] were made of polycrystalline Bi and had a hole just large enough to leave little space for stray radiation to leak from source to detector.

The behavior of the assembled samples was studied by means of the circuit shown in Fig. 4. The sample in a liquid-helium Dewar of 10-liter capacity was connected to a current supply consisting of a variable transformer supplied from the 60-Hz power line, a stepdown transformer, and a circuit of silicon-controlled rectifiers (SCR) and diodes for gating periodically half-cycles of current. The timing pulses applied to the SCR's were derived from a Tektronix type 555 dual beam oscilloscope. Its time base units were both of the type which allows separate arming and triggering of the sweep. The first of these was armed by a generator with repetition rate of about 1 pulse/sec and triggered from the 60-Hz line. A properly phased output pulse was generated (with a duration given by the sweep setting) which

[8] Equation (7) of Ref. 1, which gives the analogous expression for $k\pm$, contains two $\pm$ signs, the second of which was inadvertently reversed.

[9] G. E. Smith, L. C. Hebel, and S. J. Buchsbaum, Phys. Rev. **129**, 154 (1963).

[10] R. N. Zitter, Phys. Rev. **127**, 1471 (1962).

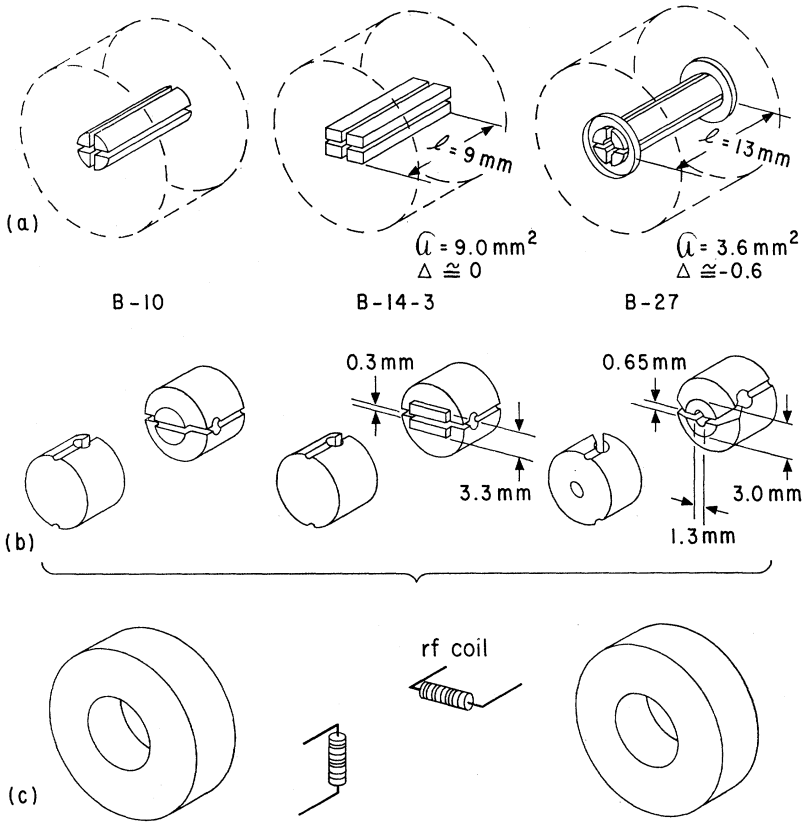

FIG. 3. (a) Current-carrying portion of a solid block (dashed lines) acting as a waveguide. (b) Contact geometries used to produce shapes in (a). (c) Coils and end blocks used in assembly of a completed structure.

triggered one or both SCR's—corresponding to one or both directions of current flow—producing, thereby, single or multiple, half or whole cycles. The second time base unit in conjunction with sweep delay and suitable unblanking pulses was used to generate a sweep for examining the waveform.

IV. EXPERIMENTAL RESULTS AND INTERPRETATION

A. Wave Propagation and Waveguide Cutoff

The transmission amplitude response of sample B-10, for wave frequencies of 5, 50, and 500 kHz and for a field of 350 Oe, are shown in Fig. 5. The signal envelope fits the pattern described in connection with Fig. 2; the decrease in amplitude at 320 A is thought to be the result of nonlinear effects which set in when the absolute instability occurs. The most significant feature of Fig. 5 is the near constancy of the threshold for amplitude increase over the range of frequency, occurring at an observed current defined as I_{c0}. This lack of frequency dependence agrees with the waveguide cutoff current calculated in Eq. (10).

The magnetic field dependence of the observed cutoff was studied using sample B-14-3. The observed cutoff current I_{c0} for both directions of transmission is shown in Fig. 6. The criterion used in estimating I_{c0} was that it is the current at which the increase in amplitude is about 1% of the increase at $2I_{c0}$. The linear relation between j_c and H_z given by Eq. (10) (for $\Theta=0$) is shown by the

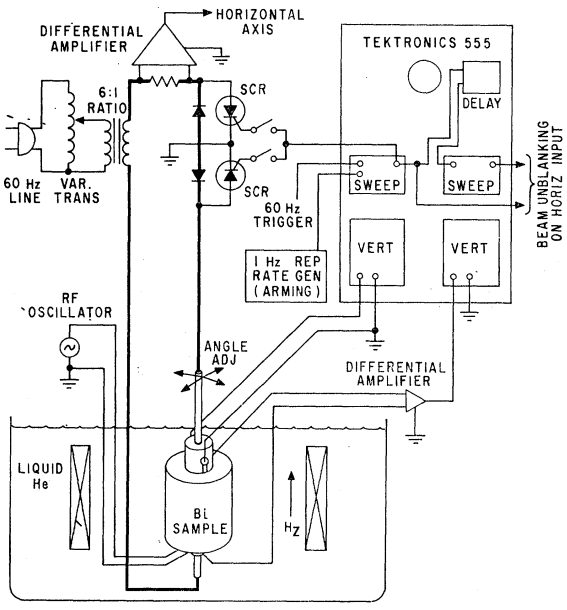

FIG. 4. Circuit diagram.

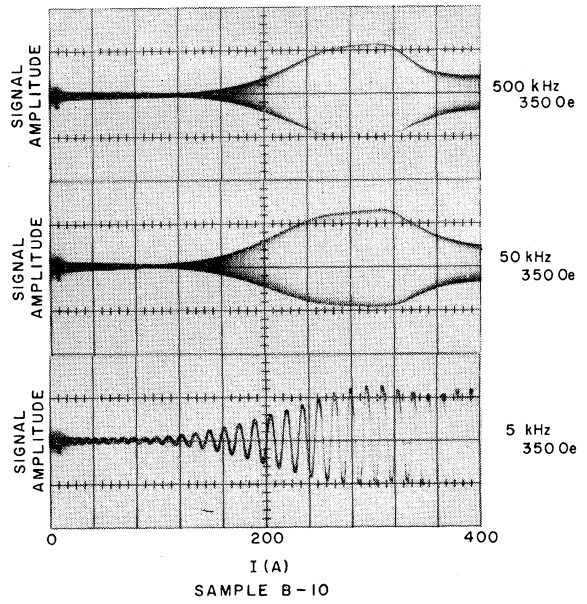

FIG. 5. Response of sample B-10 at three frequencies.

dashed line calculated from the waveguide dimensions given in Sec. III. The transverse wave number

$$k_\perp = \sqrt{2}\pi/d \tag{14}$$

used in calculating the slope is appropriate for a square metallic waveguide of transverse dimension d. The solid curves were calculated from Eqs. (8) and (14) and the expression

$$\ln A = \mathrm{Im} k_{z\pm} z. \tag{15}$$

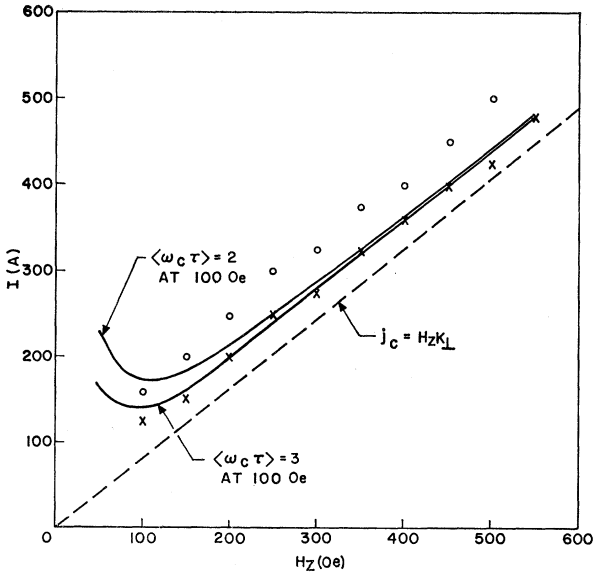

FIG. 6. Observed threshold current of sample B-14-3 for the two directions of propagation (points ⊙ and x) and calculated threshold for two values of $\langle\omega_c\tau\rangle$ (solid curves).

The same criterion (1% of A at $2I_{c0}$) as used in the experimental determination of I_{c0} was applied. The only adjustable parameter was the value of $\langle\omega_c\tau\rangle$ of which two values are shown in Fig. 6. The larger value gives the better fit. Over the range of Fig. 6, the effect of the parameter Θ (with the arbitrary assumption $\langle\langle\omega_c\tau\rangle\rangle \simeq \langle\omega_c\tau\rangle$) was found to have no appreciable effect on the calculated cutoff.

The agreement between theory and experiment for wave propagation in one direction is quite good, but there is a deviation for the opposite direction. The reason for the experimental difference between the two directions is not well understood, although there was some indication of a slight phase beating between the long-wavelength damped Alfvén waves (transmitted partially through the surrounding heat sink) and the waveguide waves. The crystallographic direction of the current, which was variable in sample B-14-3, also appeared to influence slightly the relative values of I_{c0} for the two directions (see also Fig. 10).

The curve calculated for the value $\langle\omega_c\tau\rangle = 3$ at 100 Oe gave the best fit to the cutoff data. With this same value, Eq. (8) also predicts with reasonable accuracy the signal amplitude between cutoff and the instability threshold (i.e., regions C and D). The observed results and the calculated signal envelopes for four values of H_z are shown in Fig. 7. While the absolute amplitude of the signal is not known, the relative amplitudes for the four values of H_z are as noted in Fig. 7 and only one adjustment was made to fit all four curves. The agreement, particularly in changes in amplitude with variation of H_z, is seen to be quite good in each case over the range I_{c0} to approximately $2I_{c0}$ (the shaded areas in the calculated response). Since we find agreement with essentially no further adjustment, we believe that simple wave propagation is quite well understood. The waves achieve very nearly the properties of lossless infinite-medium waves, as can be shown by calculating the over-all attenuation and angle θ for the case of Fig. 7(d) with 600 A applied; the wavelength in that case is 3 mm, and after traveling 3 wavelengths (9-mm sample length) the wave has suffered a calculated loss in amplitude of 37%. The angle the wave vector makes with the waveguide axis is only about $\theta = 3°$.

With this freely propagating wave picture in mind, we would expect to find the *shape* of the observed amplitude to come into better and better agreement with theory as H_z is increased. The result of Fig. 7(d) shows a significant difference in shape between theory and experiment. A likely interpretation of this difference is that at currents possibly as low as 400 A, the electron drift velocity exceeds the velocity of sound so that emission of phonons can result. The bias current-voltage relation already seen to be kinked in Fig. 7 has been observed in other data to exhibit a hysteresis which can become quite pronounced [see also the discussion of Fig. 10(a) below]. The corresponding de-

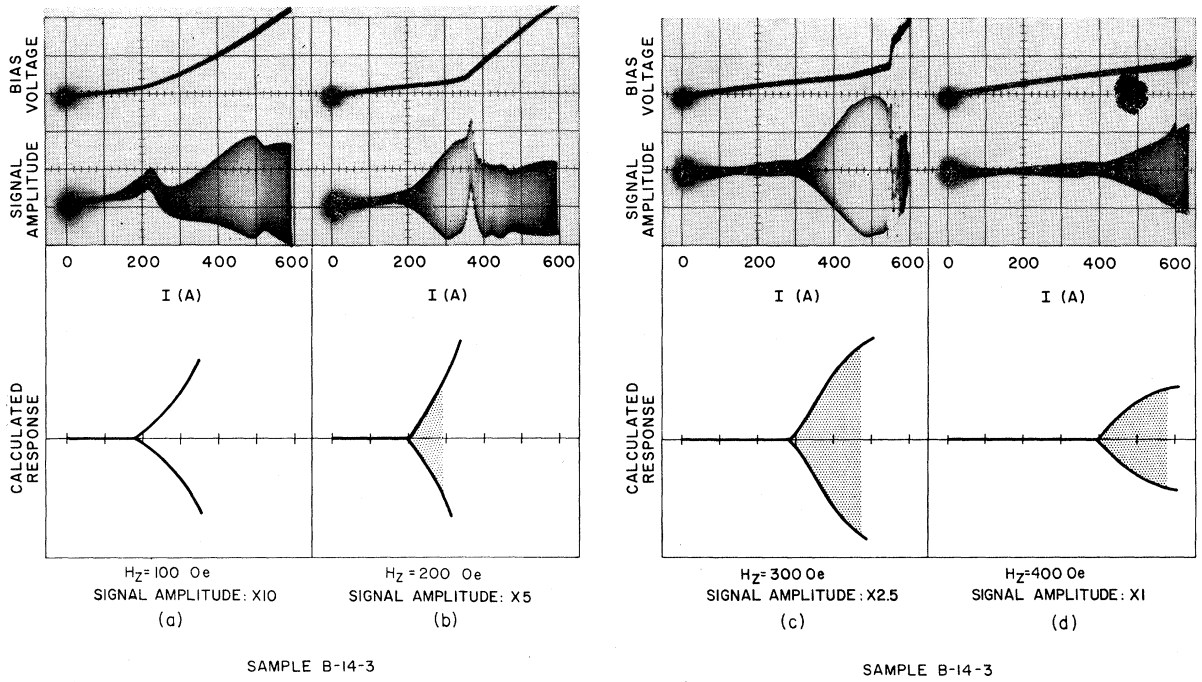

FIG. 7. Bias voltage and observed and calculated amplitude response of sample B-14-3 for 4 values of field, (a)–(d). Note change in relative signal amplitude in parts (a)–(d). Shaded portion of calculated curves indicate region of applicability.

crease in mobility (i.e., in $\langle\omega_c\tau\rangle$) would result in an amplitude response more like that observed in Fig. 7(d).

B. Amplification and Absolute Instability

At currents approximately twice I_{c0}, an oscillatory voltage is observed, which is most clearly seen in Fig. 7(c). In Figs. 7(a) and 7(b), an effect is also observed at about $2I_{c0}$, although it is more in the form of a baseline wiggle, while in Fig. 5 it shows up only as a decrease in transmitted signal amplitude. These effects are interpreted as the absolute instability mode of oscillation. Sample B-14-3 with $\Delta=0$ should give rise to absolute instability with a zero oscillation frequency as predicted by Eq. (21) of Ref. 2. An interpretation of the nonzero value in Fig. 7(c) in terms of phonon emission is given in Sec. V.

Sample B-27 exhibits this absolute instability more readily because of the cancellation of the major part of the self-magnetic field H_φ induced by the sample current I. The central-wire current I_w, when adjusted to oppose I at a magnitude $I_w=\frac{1}{2}I$, reduces the net H_φ and instability is observed at significantly lower currents than with $I_w=0$. In Sec. V, we will discuss the direct effect of I_w, as measured by the net self-magnetoresistance, as well as the threshold for instability with $I_w=0$ for this sample.

Amplification, which also occurs for $\Delta\neq0$, and absolute instability are clearly evident from the data on sample B-27 with $H_z=100$ Oe, shown in Fig. 8. In Fig. 8(a), the coil response at the sample end at which electrons arrive is shown to exhiblt an abrupt onset of oscillation at $I=90$ A. The threshold current calculated using Eq. (13) and the dimensions shown in Fig. 3 is equal to a like value of 90 A. The assumption is made here that Eq. (2) applies even in the presence of the central hole containing the stranded copper wire. We appeal to the justification that the disturbance is largely magnetic and of low frequency and that the hole and wire are no real obstacle. Furthermore, solutions using Bessel functions of the second kind, which would allow zero field in the center, do not fit nearly so well. The frequency of oscillation is close to the value 30 kHz

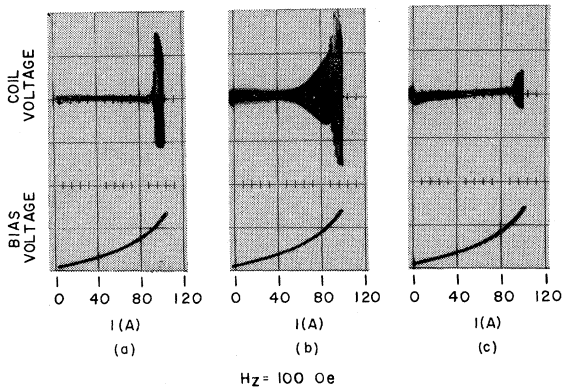

FIG. 8. (a) Self oscillation in sample B-27 with $H_z=100$ Oe and $I_w=\frac{1}{2}I$. (b) As in (a) but with 30-kHz signal applied. (c) As in (b) but with the transmission direction reversed.

reported for a different sample in Ref. 1. That value was found to be in reasonable agreement with theory.

In Fig. 8(b), a signal generator operating at 30 kHz is applied to the other coil and a transmitted signal is observed. As predicted by theory, it extends over a range of current a factor of 2 below the absolute instability threshold and has a response rising with current. Theory predicts a rise in the response to a saturated value due to improved transmission through a waveguide as well as a superimposed exponential growth due to amplification. In Fig. 8(c), the role of the two coils is exchanged and the voltage response at the end where the holes arrive is shown for the same applied amplitude of a 30-kHz signal. The reciprocity of transmission in the absence of gain is demonstrated by the equal amplitude damped Alfvén wave response at zero and small currents. At larger currents, there is almost no transmitted signal, but a self-oscillation occurs at the same current as in Fig. 8(a). Note that the amplitude of this oscillation is smaller than in Fig. 8(a), which may result from the imaginary part of the wavenumber of absolute instability as given by Eq. (16) of Ref. 2. A nonlinear amplitude limiting mechanism must also be involved. Figure 8 summarizes most of the important effects associated with the wave propagation and instability in Bi. It represents the simplest result because, at the low currents used, phonon emission does not occur and indeed the outward and return traces are nearly identical for both signal amplitude and bias voltage.

Figure 9 shows the effect of varying I_w in the neighborhood of $I_w=\frac{1}{2}I$. The lower trace in each of the three figures shows the ratio I_w/I, which in Fig. 9(c) is $\frac{1}{2}$ and, thus, corresponds to Fig. 8. The upper trace reproduces the result of Fig. 8(b) but with the current-sweep excursion limited to be less than absolute instability threshold. The optimum ratio I_w/I, that of Fig. 9(b), shows a marked increase in response which may well be close to the response that would be obtained if H_φ were exactly zero everywhere. We calculate from Eq. (11) with $\omega=0$ that the current increment δI over which the amplitude rises by a factor e is

$$\delta I=2.2(\langle\omega_c\tau\rangle/\Delta)\text{ A},$$

so that, with $\langle\omega_c\tau\rangle=3$ at 100 Oe and $|\Delta|=0.6$, we find a theoretical value of $\delta I=11$ A. This number is not directly applicable to Fig. 9(b), because the current is so low that the inherent damping at 30 kHz is important, i.e., we are operating near the upper cutoff of the amplifier and we cannot neglect the last term in Eq. (11). Between 60 and 80 A this damping factor $[\exp(-\omega enz\mathcal{A}/I\langle\omega_c\tau\rangle)]$ changes from 0.18 to 0.05. When the necessary correction is made, the experimental value of δI obtained from Fig. 9(b) is approximately 13 A. Waveguide effects have been neglected in this rough estimate.

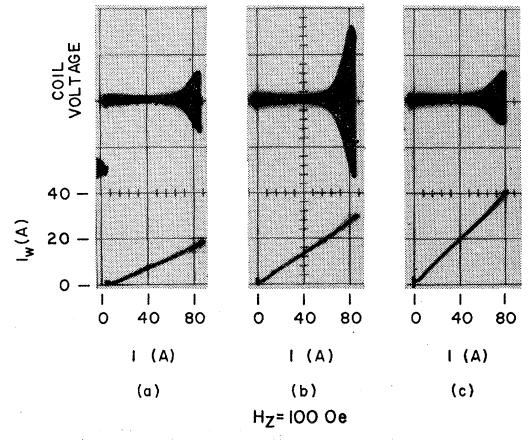

FIG. 9. As in Fig. 8(b) but with various ratios of I_w/I.

We note from Fig. 9 that, aside from an obvious depressing effect on the amplitude, H_φ also seems to be related to an asymmetry of the signal envelope above and below the base line. Figures 9(a) and 9(c) show that this asymmetry is opposite depending on the value of I_w relative to the optimum I_w.

These results on wave propagation and waveguide cutoff and on amplification and absolute instability, thus, appear to be in reasonable agreement with theory. Most of the data on these and other samples was obtained, however, when one or more of the side effects mentioned are not negligible and a proper perspective of the results of this section cannot be obtained without at least some description of their influence. In fact, the largest observed gain was obtained under conditions of phonon emission.

V. PHONON EMISSION, SELF-MAGNETIC FIELD, AND FEEDBACK EFFECTS

A. Introduction

We begin herewith a survey of additional observations which illustrate each of the three side effects and show also how these act in combination to give rise to the typical results involving wave interactions of most samples. A study of nonlinearity of the current-voltage relation of the bias terminals has made it possible to classify the occurrence of nonlinearity according to whether phonon emission or self-field occur separately or whether they occur in conjunction with instability of plasma waves. The most commonly observed experimental situations, wherein both phonon and self-field effects occur together with instability, do not lend themselves to simple quantitative interpretation. As an example, Fig. 10(a) reproduces the results of Fig. 7(c) except that the return trace is also shown. The I–V characteristic exhibits a pronounced hysteresis and the transmitted signal amplitude is also markedly affected during the retrace. The most plausible explanation in view of the rather long time duration of the hysteresis and additional data presented below is that long-lived low-frequency acoustic waves are generated, but only in

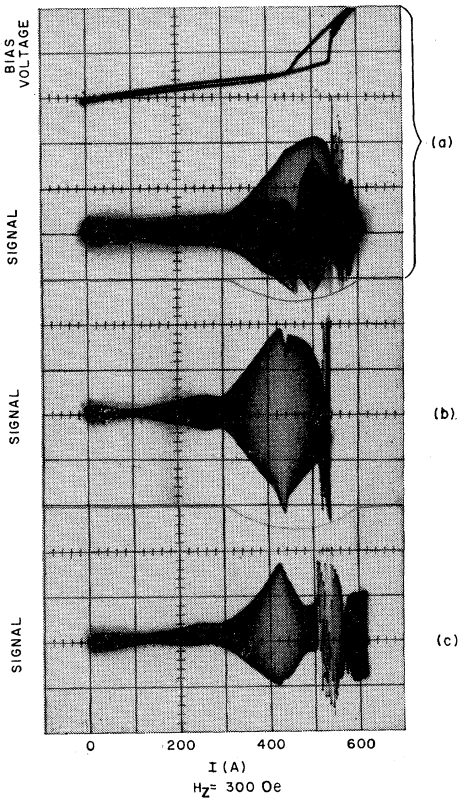

FIG. 10. Same as 7(c) but for sample angle tilted successively, up to 9° in (c). In (a), the return trace is shown superimposed on the outgoing trace. Outgoing trace only is shown in (b) and (c) and Fig. 7.

conjunction with the absolute instability. Evidence for a long duration wave is the fact that when a second half-period pulse of the 60-Hz line follows the first delayed by approximately 8 msec, there is no marked hysteresis during the second pulse (the higher slope is observed even at low currents) when the bias amplitude is sufficient to cause pronounced hysteresis in the first. The interaction between phonon emission and instability is documented below and shows evidence of a net enhancement of the instability mechanism. It will be recalled from Sec. IV that the effect H_φ was to depress plasma-wave amplitude. Which of these two effects dominates in any given situation is difficult to predict, but we might expect that at large currents the highly nonlinear effect of large amplitude acoustic flux will dominate.

Some of the complexity of the problem is illustrated by Figs. 10(b) and 10(c), wherein only the outgoing trace is shown while the crystallographic direction of the sample is tilted progressively to a maximum tilt angle of about 9° with respect to Fig. 10(a). From Fig. 3, it is evident that sample B-14-3 will maintain a nearly constant current cross section when tilted over this range of angle with respect to the field direction. This result was verified by the virtually constant low-bias conductance and the observed constancy of the waveguide cutoff threshold in Fig. 10. The observed dramatic changes in the high-current response are not understood in detail but appear to be associated with changes in the parameter Δ to a nonzero value because of the changes in crystallographic direction. The aim of the choice of crystallographic direction in Fig. 10(a) was to obtain $\Delta=0$, although this value has not been directly verified.

The value $\Delta=0$ would lead by Eq. (21) of Ref. 2 to a vanishing oscillation frequency of the absolute instability. In actual fact, however, the oscillation frequency is nonzero even in the optimum alignment data of Fig. 10(a). The phonon emission process is quite likely responsible for a value of Δ which becomes nonvanishing at high currents, and can, thus, explain this apparent discrepancy. It is noted that the fastest carriers will interact preferentially with the phonon system and that it is only their mobility that is reduced. In a complicated system like Bi, the value of Δ is then almost certainly affected. Our direct evidence that such a change in Δ takes place comes from the lower magnetic field data of Figs. 7(a) and 7(b), where the oscillation frequency is very low, since it occurs below the 400-A phonon threshold current. Indeed, in Fig. 10, the oscillation frequency does not rise until absolute instability occurs under conditions of appreciable over-all conductivity reduction (and, hence, mobility reduction), as indicated by the step in bias voltage.

Complications of the type encountered here result from the interaction of a number of simultaneous effects, the effect of the self-field not even having been discussed. Multiple interactions are preferably avoided for a more detailed understanding and, in the following, individual phenomena or simple combinations are brought out as much as possible.

B. Phonon Emission—Absolute Instability

In the foregoing, an interaction was shown between phonons and instability in a sample used for the purpose of studying waveguide effects. We present now data on samples which had much smaller current cross sections and used solid contacts with no provision for pickup coils. The smaller cross section requires a higher current density for waveguide cutoff of the absolute instability for given H_z. Phonon emission is, therefore, stronger at threshold. Also in most cases, somewhat lower H_z was used with the result that at threshold the azimuthal field was reduced; the latter, unless stated otherwise, is assumed to have no strong effect.

With the results obtained using these samples, we can show directly that the combined phonon-and-instability effect produces a much stronger interaction than either effect alone as measured by the nonlinearity of the I–V characteristic. Phonon-emission-only results are shown in Fig. 11(a) for a sample with H_z large enough (600 Oe) to raise the instability threshold above the maximum current. There are three voltage steps occurring in two

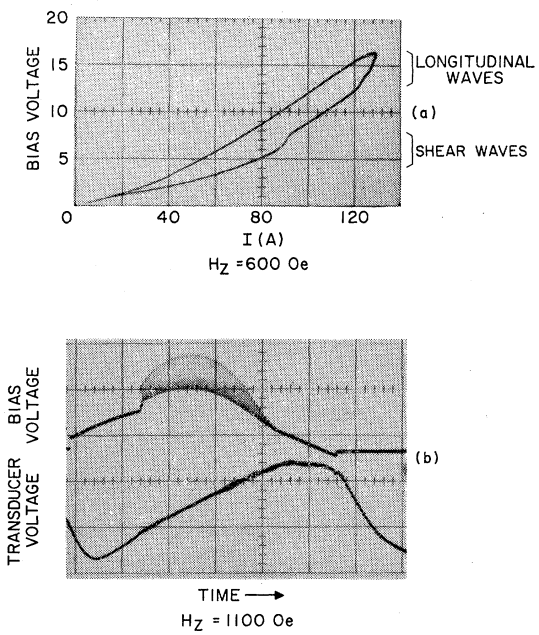

FIG. 11. (a) Current-voltage relation showing voltage steps interpreted as resulting from phonon emission. (b) Upper trace: bias voltage oscillations associated with absolute instability mode. Lower trace: output from low-frequency acoustic transducer showing persistence of oscillation after cessation of current.

groups. These are interpreted as resulting from interaction of the fastest electrons with shear waves and longitudinal waves. A quantitative fit using the mobility and known sound velocity values to the voltages or even the voltage ratios of these steps has not been made here because, in this case, H_φ is not negligible and has caused some curvature of the characteristic through self-magnetoresistance (see below). Detailed correction for this effect is very difficult, but a simple extrapolation of the low-bias slope to the current at the step leads to voltages in reasonable agreement. The crystal orientation was identical to that of sample B-27 and the longitudinal sound velocity is expected to have some lifting of the degeneracy which it has for sound waves directed along the Z axis, hence, the double step.

Direct evidence of the phonon-instability interaction was obtained from a sample on which a quartz low-frequency shear-wave transducer was placed on an end face adjacent to the contact. The time displays in Fig. 11(b) show that the sample voltage became strongly oscillatory in much the same manner as the I–V characteristic in Fig. 10(a) shows some oscillation voltage. The transducer output voltage shows an oscillatory response with a like frequency starting at the same time, but differing in that this oscillation persists even after the current has stopped. A peculiarity of the bias voltage oscillation is that its frequency of approximately 30 kHz is much less dependent on current than the j^2 dependence predicted by Eq. (21) of Ref. 2. A plausible model is that in the combined interaction the frequency is that of the strongest effect, which occurs at the peak current value. When the current decreases, this frequency continues to dominate the combined oscillation through the sound-wave persistence. The transducer output shows an apparently related beating effect during the time the current decreases to below instability threshold.

The evidence for low-frequency acoustic flux with long lifetime suggests a picture in which the sample is undergoing high-Q mechanical resonances. The possibility that suppression of this Q might reduce the interaction has not been explored experimentally.

The data in Fig. 12 show that the phonon-and-instability effect produces more pronounced nonlinearity than the phonons only [Fig. 11(a)] or absolute instability only [see, for example, Fig. 8(a)]. The sample consisted of contacts with area of 1 mm² and current was directed along the Z axis. In Fig. 12(a), H_z was held fixed at 350 Oe while the maximum current excursion was increased successively in the three traces. These traces are a rare example of variation of the characteristic with maximum current amplitude; in all such cases some relation to the sound-velocity threshold was indicated. Figure 12(b) shows the result of increasing H_z while the maximum current was held constant at the highest value of Fig. 12(a). The interpretation of these abrupt nonlinearities is that Fig. 12(a) shows the need for the undistorted I–V characteristic to exceed some critical voltage ~4 mV, while Fig. 12(b) gives a current threshold which depends on H_z. (Note the undistorted I–V characteristic is relatively unaffected by self-magnetoresistance for this small contact dimension.) As an example of how the current threshold fits the absolute instability model, we observe that, for the 570-Oe

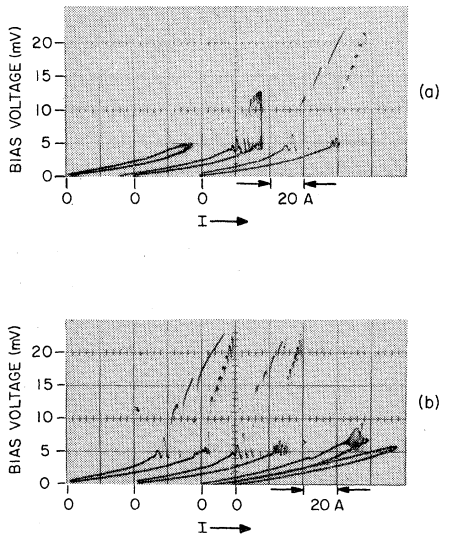

FIG. 12. (a) Development of strongly nonlinear current-voltage relation when maximum current excursion is increased (H_z=350 Oe). (b) As in (a) except that current excursion is constant and H_z has the values 350, 400, 570, and 1100 Oe.

curve, theory predicts a threshold current of 100 A. The observed oscillation is about to be quenched at this field and has a threshold of 90 A, in good agreement. The oscillations all show a distinct lower voltage limit of ~4 mV and the 570-Oe curve has a small depression at that value as well.

When the current excursion exceeds the maximum used in Fig. 12(a), a nonoscillatory characteristic forms at high current with slope equaling the extension of the return trace. Perhaps in that case the frequency vanishes in accordance with such a prediction by Eq. (20) of Ref. 2 in the limit of large growth rate and finite relaxation time. Actually, an oscillation frequency of 60 Hz is appropriate in these measurements. Some brief measurements, using pure dc, of the behavior of the high-current response appear to be in agreement with the 60-Hz results.

The data on the phonon-emission absolute instability interaction, thus, show a clear enhancement of the nonlinearity. Similar data on single crystals of Sb have also been obtained.

C. Phonon Emission—Convective Instability

Much as the presence of absolute instability leads to enhanced interaction of electrons with phonons, the interaction of convective instability and phonon emission leads to enhancement, this time most noticeably in the gain of the plasma waves. A striking example is an isolated observation on a sample (B-21) which is shown below to exhibit gain strong enough to lead to feedback oscillations. Figure 13(a) shows the transmission response of a 75-kHz signal for two settings of the maximum current excursion. In the right-hand figure, in which the maximum current has been increased incrementally, the return trace is greatly enhanced by what is assumed to be phonon emission. Although it is too complicated for detailed analysis, this result serves well to introduce the feedback results which follow later, because it was on this return trace that these oscillations were most readily observed. The variation of cross section $\mathcal{A}$ when the sample is tilted in the manner of Fig. 10, however, makes quantitative interpretation difficult.

A similar result was observed with sample B-27 with no wire current ($H_z=148$ Oe) as shown in Figs. 13(b) and 13(c). Here, the current excursion is fixed and the two figures are just separate records of identical events, one showing the outgoing the other the return trace. We see an enhancement of the 70-kHz transmitted signal and an additional increment in the region between the two voltage steps. The second step is similar to the double-voltage step of Fig. 11, which was given the interpretation of interaction with longitudinal sound waves. An alternative interpretation might result from the fact that the 8° tilt angle with respect to the Z axis makes the drift velocity of the three electron ellipsoids nonequivalent and these electrons interact separately

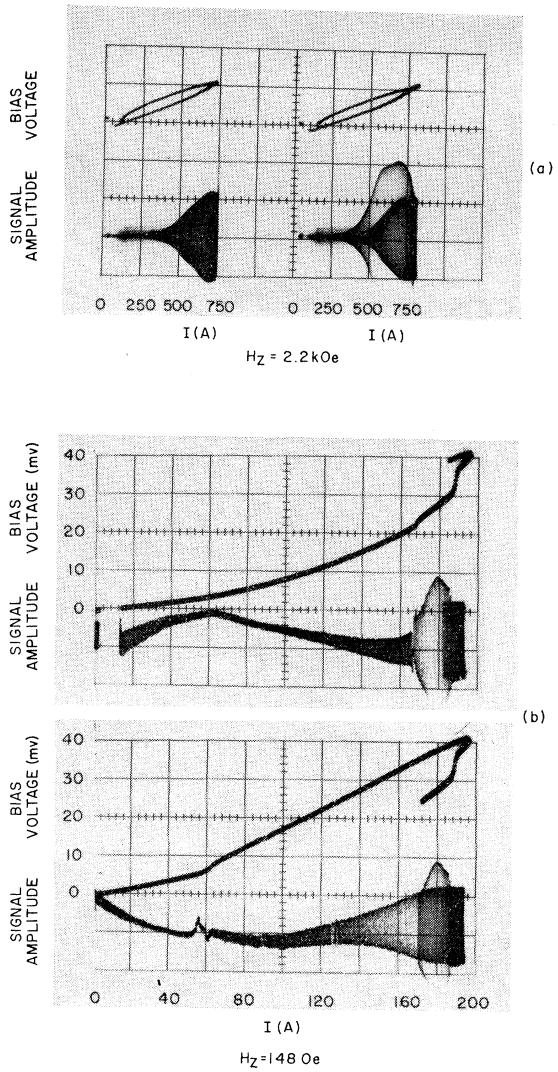

FIG. 13. (a) Bias voltage and transmission response of sample B-21 with $H_z=2.2$ kOe for two settings of maximum current excursion. (b) Upper and lower figures are outgoing and return traces, respectively, of bias voltage and transmission response of sample B-27 ($I_w=0$) with $H_z=148$ Oe.

with shear waves. This interpretation might also apply to Fig. 11(a), except that a double upper step is not to be expected. If all the current is carried by electrons, as may be inferred from the nearly 30-to-1 ratio of electron and hole mobilities given by Zitter,[9] the threshold current is $I=195$ A (using $V_s=1.13\times10^5$ cm/sec). Variations in cross-sectional area and in V_s, resulting from the 8° tilt, and the effect of self-magnetoresistance may explain the discrepancy with the observed value of 170 A. In Fig. 15(a) below, similar, but smaller, kinks for this sample generally occur at 180 A, already in better agreement.

We may speculate on the pronounced hysteresis of Fig. 13 compared with, say, the 100-Oe curve of Fig. 15(a). There is the possibility that the plasma-wave

amplification affects the sample voltage through its requirement of extra power. The kink in the return trace of Fig. 13(b) at 60 A, for example, corresponds quite closely to the waveguide threshold. [By comparing with Fig. 8(b), a threshold of 66 A results.] Also, some samples showed broadband noise on the voltage when threshold was reached and in others, when feedback oscillations were being examined as explained below, the bias voltage showed oscillations in response to an externally applied low-level signal. A detailed interpretation is beyond our scope, but one fact is clear: Phonon interaction can enhance transmitted waves.

A final result on sample B-27 leaves no doubt of this interaction and also illustrates the experimental situation in which maximum nonreciprocal gain was observed. Figure 14 shows a 20-kHz transmitted signal when $H_z=50$ Oe and the current is swept in both directions. The abrupt rise in signal starts at the same current ($\sim$165 A) as that in Fig. 13. A small-amplitude absolute-instability signal is observed when $I=\sim$250 A in Fig. 14(b). When H_z was lowered to 25 Oe, a similar result was obtained over the same current range with slightly larger signal growth with current. The waveguide cutoff of either wave propagation or instability for these fields lies below 50 A so that the abrupt signal onset again proves that phonons are aiding the gain here. Under similar conditions, the insertion loss of the whole structure, input-to-output coil terminals, was measured to be of order unity. Since losses contributed by the signal-coupling geometry are estimated to be of order 10^2–10^3, gains of this order must have existed in the Bi.

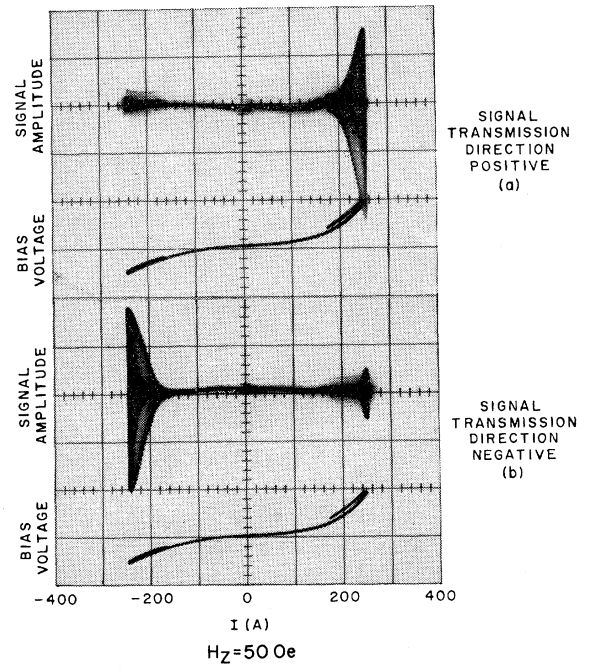

FIG. 14. Signal amplitude and bias voltage of sample B-27 when the signal is transmitted in the two opposite directions, parts (a) and (b).

D. Azimuthal Self-Magnetic Field (H_φ) Effects

The azimuthal magnetic field produced by a current I flowing within a radius r is at that radius

$$H_\varphi|_r=I/2\pi r.$$

The condition for wave propagation just below onset of absolute instability, for the case of a cylindrical waveguide, is given by Eq. (13):

$$H_z=j/2k_1=I/(2.405\times 2\pi r).$$

The ratio of these magnetic field components at radius r is then

$$H_\varphi/H_z|_r=2.405.$$

This rather large value shows the need for H_φ to be considered, although it is true that most of the energy would be transported by the waveguide in the center where H_φ vanishes. For our specific contact geometry, no simple generalization like this can be made because often no current flows at the center of the waveguide, although the resulting reduction in current-carrying area tends to make the ratio H_φ/H_z smaller.

The direct influence of H_φ on the carrier motion is an inward velocity V_{in} for both electrons and holes. One consequence is that carriers with suitable mobility anisotropy may exceed the sound velocity by virtue of V_{in} rather than the longitudinal velocity V_z. The phonon-emission problem under conditions of large H_φ is, therefore, very complex and has not been investigated. Another consequence of V_{in} might be the production of a "pinch" effect characterized by a nonequilibrium carrier concentration at the center, but no direct evidence for its existence was obtained in these experiments. What was observed was a pronounced magnetoresistance for current flow along in the z direction. Since this resistance is largest at the periphery of the waveguide, there is a tendency for the current to crowd toward the center, although without disturbing the actual density of carriers. Self-magnetoresistance has been observed previously[11] in Bi at 77°K.

The I–V relation of sample B-27 for $I_w=0$ at 5 values of H_z is shown in Fig. 15(a). The relation is strongly curved but shows a linear portion at low currents. The slope at small currents increases modestly with applied H_z and at $H_z=0$ leads to a resistance [which is more accurately determined from Fig. 15(b)] of 1.7×10^{-5} Ω. Using the sample length $l=1.3$ cm and area $\mathcal{A}=3.6\times10^{-2}$ cm^2 and the published room-temperature resistivity of Bi, this value of sample resistance corresponds to a conductivity ratio of 320, a value close to that measured by conventional means. At high currents (the maximum current excursion of the five curves is about the same), there is an unexplained dependence of

[11] T. Hattori and S. Tosima, J. Phys. Soc. Japan **20**, 44 (1965).

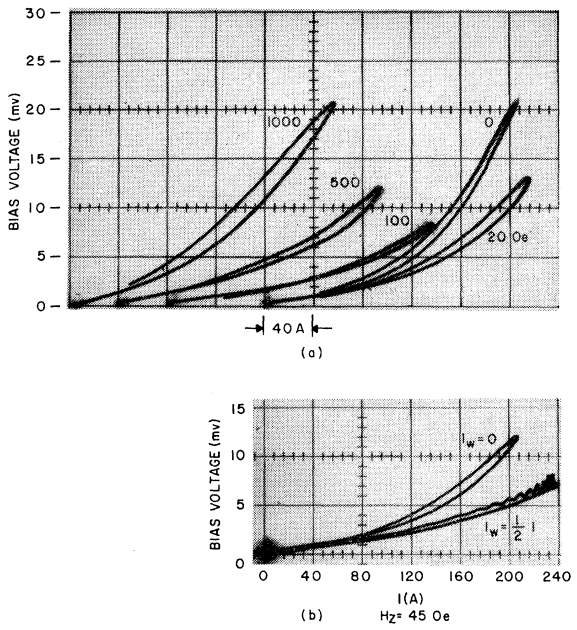

FIG. 15. (a) Bias current-voltage relation of sample B-27 for various fields and $I_w=0$. (b) Same as (a), 45 Oe with $I_w=0$ and $\frac{1}{2}I_s$.

the curvature on H_z, with a minimum curvature occurring between 20 and 100 Oe. The hysteresis effect is again attributed to phonon emission.

Figure 15(b) shows the I–V relation, when $I_w=0$ and $\frac{1}{2}I$ at 45 Oe. The wire current was obtained from an independent circuit duplicating that used to pass half-cycles of the 60-Hz line through the sample. Both circuits were connected as well to an additional common variable transformer. By adjusting the individual variable transformer settings, any desired current ratio could be obtained. It was found that the ratio $I_w/I=\frac{1}{2}$ gave very nearly the most linear relation. An increase of I_w to a value somewhat less than $2I$ gave the expected result of a return to approximately the $I_w=0$ curve and increases beyond gave a more sharply curved result.

E. Feedback Oscillation

Sample B-21 used for this study was constructed like B-14-3 except for the following changes. The crystallographic direction corresponded to that of sample B-27. The waveguide length was greater at 22 mm, while the over-all cross-sectional dimension of the waveguide was 3.75 mm and the slot width 0.75 mm. The area $\mathcal{A}$ appropriate for converting current to current density is, therefore, 9.0 mm^2. The length of the contact stripe was only 5 mm. As a result of the long sample length and near equality of contact length and width, it was possible and, indeed, common that the sample tilt angle in the field caused a reduction in $\mathcal{A}$ below 9.0 mm^2.

The main difference between samples B-21 and B-27, aside from the extra length of the former which should produce enhanced over-all gain, is in the depression or "moat" around the current contacts of sample B-27 [see Fig. 3(a)]. Without this moat, feedback oscillations are set up wherein damped Alfvén waves in the surrounding material are the return path. The moat serves the purpose of preventing coupling to the damped Alfvén waves at the waveguide ends. (The oscillations were also suppressed in another sample by cutting slots in heat sink.)

One feature of the oscillations, which immediately sets them apart from the absolute instability oscillations, is the possibility of marginally suppressing them by critical adjustment of I and H_z. When a signal generator is applied to one coil, at a frequency equaling that which the oscillation would have had, a sharply peaked response appears in the other coil centered at the same value of current as was the oscillation. A different frequency, however, would give a different value of current. Since the signal can be applied to either coil to cause such a response, the transmission appears to be essentially reciprocal in spite of the fact that nonreciprocal amplification is involved.

The four return traces in Fig. 16(a), taken with $H_z=700$ Oe, correspond to frequencies of 25, 50, 75,

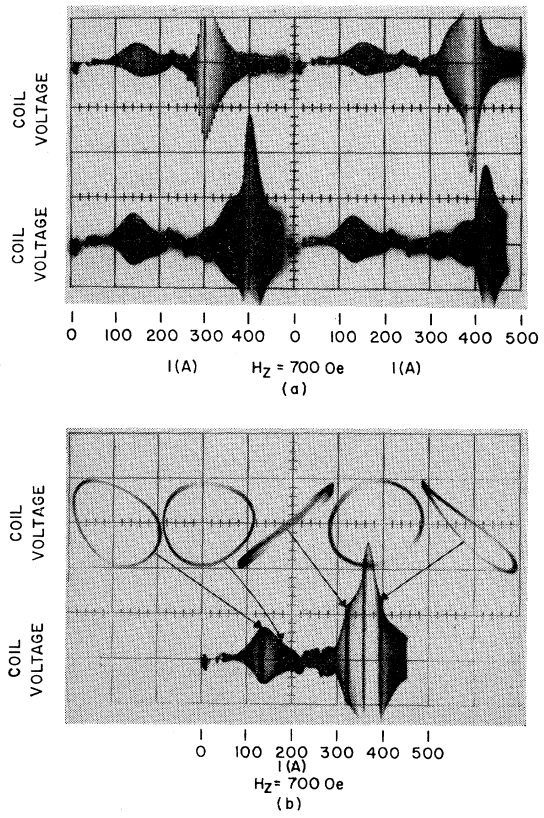

FIG. 16. (a) Coil voltage of sample B-21 at $H_z=700$ Oe for four frequencies, 25, 50, 75, and 100 kHz. (b) 50-kHz response showing also the phase of the enhanced portions.

and 100 kHz and show a sharp peak which progresses to higher currents with frequency. In Fig. 16(b), the 50-kHz result is examined for the relation between output phase and phase of the generator. The five Lissajou's figures, corresponding to the enhanced portions of the output-amplitude response, were obtained by making the appropriate change in vertical sensitivity and applying the generator signal directly to the horizontal axis. The results illustrate clearly that at each side of the sharp maximum there is a 90° phase shift relative to the phase at the peak. There are several distinct peaks in Fig. 16(a) in the range 300 A $<I<$450 A which appear to correspond to several phase matching conditions.

A link in the feedback loop is the damped Alfvén wave. At 100 kHz, we obtain[6] a wavelength $\lambda=(0.73\langle\omega_c\tau\rangle)^{1/2}$ cm. A value of $\langle\omega_c\tau\rangle\simeq 14$ at 700 Oe is not unreasonable, so that $\lambda=32.5$ mm. It is clear that for a 22-mm sample these waves have a slow dependence of phase on frequency. Since at a given frequency the damped Alfvén wave response is constant and independent of current, the amplitude at the observed peaks in the range 300 A $<I<$450 A is representative of the amount of gain in the waveguide. An exponential dependence is predicted and appears also to be observed. Theory predicts a constant gain below some frequency and above it a decrease proportional to frequency. In addition, the efficiency of damped Alfvén wave feedback falls as the square root of frequency. Some of these effects are evident in the data.

VI. DISCUSSION

Having observed the amplification in Bi, we are quite naturally led to speculate on similar effects in other materials and configurations. Appendix B is concerned with the relation between material parameters and the characteristics of the amplification, particularly $\omega_{\max}$, when the thermal considerations pertinent to continuous operation are taken into account. The appendix shows Bi to be a nearly ideal choice because of its high mobility. We shall, therefore, give some of the properties of an idealized Bi structure, neglecting the phonon-emission problem, and speculate also on the mechanism of enhancement of gain with phonons and some of the consequences.

From Eq. (11), we see that for $\omega\ll\omega_{\max}$ the amplifier gain is independent of ω. Such flat response is usually very desirable, but the dispersion of this amplifier is so pronounced that normal broad band operation is probably not practical. The dispersive character is shown by the time delay Δt of a given phase front in passing through a structure of length z_0:

$$\Delta t\equiv z_0/V = (z_0/\omega)\,\mathrm{Re}|k| = z_0 J/\omega H_z. \tag{16}$$

The delay increases with decreasing frequency so that the phase relations among different frequency components of a broad band signal will become disturbed. The amplifier will, however, give a constant phase angle shift over its bandwidth, dc to possibly microwave frequencies. In fact, amplification is not really necessary in order to realize the latter property.

It may, furthermore, be possible to realize large time delays at low frequencies if the gain is adjusted to just overcome the loss and a large z_0 is used. For an amplifier with $z_0=10$ cm, operating at 50 G with a current density such that phonon emission is just avoided, a value $f\Delta t\simeq 350$ is obtained. A 10-Hz signal will, therefore, take 35 sec to travel through this structure.

We now calculate the required condition for amplification in Bi with a cutoff of 1 GHz at 50 Oe. With 50 Oe applied along the Z axis, the electron and hole cyclotron frequencies are roughly at 2 GHz. Our calculation is to be considered only a rough approximation because we are satisfying only the most essential conditions, e.g., $\omega<\omega_c$. Using Eq. (B3) with $\Delta=-0.6$, we find waveguide radius $r=8.3\times10^{-4}$ cm. From r, we find $j=2.3\times10^5$ A/cm^2 and $I=0.52$ A. In steady-state operation, Eq. (B2) gives $P_A=9.2$ W/cm^2, so that, from the known thermal conductivity, a temperature gradient of 1.5°K/cm would be required. These numbers all appear to be very modest until one realizes that the electron drift velocity is about 5×10^6 cm/sec. Phonon-emission effects may then be expected to dominate and these are usually accompanied by a drastic reduction in carrier mobility. It may be possible to retain a good mobility by pulsing for short periods to avoid the large-amplitude phonon buildup or by lowering the mechanical Q of the sample. The adiabatic rate of temperature rise for pulsed operation is 2.3°K/μsec for this example. An additional problem is the self-magnetic field of the current which in this example has a value of 125 Oe at the surface of the waveguide.

The amplification situation in the presence of phonon emission may also not be completely without virtue in an appropriate situation, e.g., one wherein the total buildup of acoustic flux is controlled. As we have seen in Sec. V, gain is enhanced by the emission and $\omega_{\max}$ may be raised with the result that the other requirements are somewhat eased.

We now consider the mechanism by which phonons enhance the gain. In brief, gain occurs when the electrons with velocity V_z exceeding phase velocity V_φ experience more collisions than those with $V_z<V_\varphi$, i.e., we normally require $V_d>V_\varphi$. Now when V_d also exceeds V_s, and also $V_s>V_\varphi$, the electrons with $V_z\sim V_s$ experience enhanced collisions and gain is enhanced. In the weak damping limit $\omega_c\tau\gg1$, Eq. (52) of Ref. 2 states the requirement for gain more precisely, i.e., $V_\varphi<\Delta V_d$. The condition is seen to stem from Imk^2 of Eq. (1) of Ref. 2, and, in fact, traces back to Eq. (A2) of Ref. 2. The latter states that there will be one carrier species (electrons here) for which $\omega-k_\pm V_d<0$ so that, after rationalization, there is a term proportional to $i/\omega_c\tau$ which

changes sign when $\omega/k_{\perp}=V_d$. This sign reversal can be traced also to Eq. (A1) of Ref. 2 and there it is easy to see that when $\tau=\tau(V_z)$ there is a weighting effect under the conditions described above. In other words, when considering the damping we should not calculate the center of gravity of particle velocities but instead compute the center of gravity of collision events. When $V_d>V_s$, these centers do not necessarily coincide.

Extrapolation to a situation wherein this effect is optimized will serve to illustrate the point. Consider a Fermi distribution of particles for which $\tau(V)$ is such that near $V=V_F$ there is an abrupt decrease in τ. Further, assume helicon waves propagate with $V_\varphi \ll V_F$, as is often the case in metals. We now apply a drift such that $V_d \ll V_\varphi$ and find that there will be gain when $\partial\tau/\partial V$ is a sufficiently large negative. The reasoning is simply that the particles with $V_z=+V_F$ will contribute a negative amount to the integral of Eq. (A1) of Ref. 2, while those with $V_z=-V_F$ give a positive contribution. The offset in velocity, however, will make the contribution of the $V_z>0$ particles exceed that of the others. The large value of V_F, furthermore, assures that these contributions are important in the over-all integral. The onset of "open orbits" may provide a suitably abrupt relation $\tau(V_z)$ to make this effect easy to observe.

VII. CONCLUSION

Circularly polarized low-frequency waves, with some properties like helicon waves and other properties quite different, have been studied in single crystals of Bi at 4.2°K when parallel current and magnetic field are applied. The threshold for their occurrence, in agreement with theory, depends on the ratio of current and magnetic field and is further modified by collision damping. A simple set of "metallic-boundary" conditions was found to be adequate for the waveguide description when used in conjunction with the dielectric tensor derived by Misawa. The waveguide cutoff condition was found to be independent of frequency over a wide range, in agreement with the theoretical prediction that the waves have a constant wavelength from dc to frequencies as high as microwaves under some conditions.

For appropriate crystallographic orientations, in particular a direction 8° off the Z axis along a $-Y$ direction, amplification of these waves was observed. According to theory, the orientation controls the net damping by suitable average of the electron and hole mobilities which are highly anisotropic in Bi. The waveguide cutoff studies were made with a sample oriented for minimum gain and the strong orientation dependence of the gain was thereby confirmed. The magnitude of the gain in the favorable direction was in approximate agreement with the predicted value.

At currents close to twice those required for waveguide cutoff, theory predicts onset of an absolute instability mode of oscillation. The quantitative value of this current ratio has been amply confirmed for experimentally observed oscillations, although the frequency of the oscillation was found to vary with the particular circumstances. Nevertheless, a qualitative understanding of the frequency variation has been obtained in terms of one of the three side effects present in these samples, namely, emission of phonons by electrons streaming faster than the lattice sound velocity.

The first of the side effects was the azimuthal self-magnetic field of the current. The latter was minimized by a special sample geometry wherein a coaxial wire was used to carry an opposing current. By minimizing this field, it was learned that it has a depressing effect on wave amplitude. The second side effect, the phonon emission, on the other hand, appears to be able to enhance the amplification. A qualitative explanation of this effect has been given and by analogy an amplifier is proposed wherein open orbits cause a velocity-dependent relaxation time which acts on helicon waves in a metal to give gain for very small drift velocities. The maximum gain, observed in Bi under conditions of phonon emission, was estimated at 10^2–10^3. The third side effect, feedback oscillation within the sample, was observed but was eliminated by suitable choice of geometry. The characteristics of the amplification were evident also from the oscillation data.

Since Bi with its high carrier mobility appears to be a nearly ideal choice of material for a study of amplification of this type, an idealized case has been calculated for amplification at 1 GHz. If phonon-emission degradation of the mobility and the self-magnetic field could be avoided, the power dissipation requirements would be quite modest, but these effects appear at present to preclude operation at that frequency.

ACKNOWLEDGMENT

The author gratefully acknowledges the technical assistance of W. A. Nordland in preparing the samples and making the measurements.

APPENDIX A: DERIVATION OF DISPERSION RELATION FROM MISAWA'S DIELECTRIC TENSOR

The dispersion relation is derived here for wave propagation at an angle θ relative to the common direction of magnetic field $\mathbf{H}$ and current density $\mathbf{j}$. Misawa[7] has given the general dielectric tensor for parallel $\mathbf{j}$ and $\mathbf{H}$. We simplify and approximate his result to apply only to a compensated plasma in the low-frequency limit ($\omega \ll \omega_c, \tau^{-1}$), paying particular attention to its applicability at low magnetic fields (i.e., $\omega_c\tau \sim 1$). It is our intention to derive a correction factor in terms of θ to the dispersion relation derived in Ref. 2 (Appendix A) and, thus, make the latter applicable in a waveguide directed parallel to $\mathbf{j}$ and $\mathbf{H}$. In Ref. 2, the dispersion relation was made applicable at low magnetic fields by appropriate definitions of certain parameters, such as the current density, by specifically including in them

factors of the form $[1+(\omega_c\tau)^{-2}]^{-1}\equiv(1+W)^{-1}$. Since the origin of the dispersion relation is readily traced to the tensor elements, similar definitions can be made therein. We now rewrite the tensor elements derived by Misawa in his Eqs. (A42)–(A49) using the notation of Ref. 2 by assuming that the local limit applies and by neglecting in the denominators any Doppler-shifted frequency terms appearing squared in direct comparison with ω_c^2 or τ^{-2}.

$$\epsilon_{11}=\epsilon_{22}=k_0^{-2}\sum_s \frac{e_s n_s}{\omega_{cs}H_z} \times \frac{(\omega-\mathbf{k}\cdot\mathbf{V}_s)(\omega-\mathbf{k}\cdot\mathbf{V}_s+i/\tau_s)}{(1+W_s)}, \quad \text{(A1)}$$

$$\epsilon_{33}=-k_0^{-2}\sum_s \frac{\omega e_s n_s}{H_z}\frac{(\omega+i/\tau_s)\omega_{cs}}{(\omega-\mathbf{k}\cdot\mathbf{V}_s+i/\tau_s)^2}, \quad \text{(A2)}$$

$$\epsilon_{12}=-\epsilon_{21}=ik_0^{-2}\sum_s \frac{e_s n_s}{H_z(1+W_s)}(\omega-\mathbf{k}\cdot\mathbf{V}_s), \quad \text{(A3)}$$

$$\epsilon_{13}=k_0^{-2}\sum_s \frac{e_s n_s}{\omega_{cs}H_z}\frac{\sin\theta\, kV_s(\omega-\mathbf{k}\cdot\mathbf{V}_s+i/\tau_s)}{(1+W_s)}, \quad \text{(A4)}$$

$$\epsilon_{31}=k_0^{-2}\sum_s \frac{e_s n_s}{\omega_{cs}H_z}\frac{\sin\theta\, kV_s(\omega-\mathbf{k}\cdot\mathbf{V}_s)}{(1+W_s)}, \quad \text{(A5)}$$

$$\epsilon_{23}=-ik_0^{-2}\sum_s \frac{e_s n_s}{H_z(1+W_s)}\sin\theta\, kV_s, \quad \text{(A6)}$$

$$\epsilon_{32}=ik_0^{-2}\sum_s \frac{e_s n_s}{H_z(1+W_s)}\frac{\sin\theta\, kV_s(\omega-\mathbf{k}\cdot\mathbf{V}_s)}{(\omega-\mathbf{k}\cdot\mathbf{V}_s+i/\tau_s)}, \quad \text{(A7)}$$

where $k_0=\omega/c$, $k=|\mathbf{k}|$, and subscript s runs over the carrier species. For simplicity, e_s, ω_{cs}, and V_s ($\equiv j_s/e_s n_s$) are assumed carry the sign of the carrier charge.

In order to obtain a suitable approximate form of the dispersion relation applicable to a compensated plasma at low frequencies, we make the following approximations and comparison of terms. Introducing the anisotropy factor Δ from Ref. 2, and neglecting the Alfvén wave term in ϵ_{11}, which is the $(\omega-\mathbf{k}\cdot\mathbf{V}_s)^2$ dependence,

$$\epsilon_\perp\equiv\epsilon_{11}=\epsilon_{22}\simeq ik_0^{-2}\frac{\omega en-\Delta\cos\theta\, kj}{H_z\langle\omega_c\tau\rangle}. \quad \text{(A8)}$$

Since ϵ_{12} can be written as

$$\epsilon_{12}=ik_0^{-2}(\omega e\delta n-\cos\theta\, kj)/H_z, \quad \text{(A9)}$$

we can define for Bi, since $\delta n=0$,

$$\epsilon_x\equiv-i\epsilon_{12}|_{\delta n=0}=-k_0^{-2}\frac{\cos\theta\, kj}{H_z}. \quad \text{(A10)}$$

Furthermore,

$$\epsilon_{13}=\tan\theta\,(\epsilon_\perp-\epsilon_\omega), \quad \text{(A11)}$$

$$\epsilon_{23}=i\tan\theta\,\epsilon_x, \quad \text{(A12)}$$

where

$$\epsilon_\omega\equiv ik_0^{-2}(\omega en/H_z\langle\omega_c\tau\rangle). \quad \text{(A13)}$$

In the limit of low frequency and small wave number we may write

$$\epsilon_{33}\cong ik_0^{-2}(\omega en/H)\langle\langle\omega_c\tau\rangle\rangle, \quad \text{(A14)}$$

where

$$\langle\langle\omega_c\tau\rangle\rangle=(en)^{-1}\sum_s e_s n_s\omega_{cs}\tau_s. \quad \text{(A15)}$$

The ratio $\epsilon_\omega/\epsilon_{33}$ is, therefore,

$$\epsilon_\omega/\epsilon_{33}=1/\langle\omega_c\tau\rangle\langle\langle\omega_c\tau\rangle\rangle. \quad \text{(A16)}$$

The remaining elements ϵ_{31} and ϵ_{32} are normally small compared with ϵ_{33}, as shown by following dimensional comparison. Equation (A5) shows that ϵ_{31} consists of two sums. The sum containing ω will be the net difference between the total electron and total hole contributions, while the second sum will be their total contribution. Neglecting the former, we find that

$$\tan\theta\frac{\epsilon_{31}}{\epsilon_{33}}\cong\frac{(k_\perp\bar{V})^2}{\omega\langle\omega_c\rangle}\frac{1}{\langle\langle\omega_c\tau\rangle\rangle}\ll 1, \quad \text{(A17)}$$

where $\bar{V}$ is a suitably defined average carrier velocity, $\langle\omega_c\rangle$ is an average cyclotron frequency, and $k_\perp=k\sin\theta$. For typical values of maximum velocity and minimum waveguide diameter, the maximum value of $k_\perp\bar{V}$ is about 2×10^6 rad/sec, while $\langle\omega_c\rangle$ is typically 10^{10} rad/sec at fields for which $\langle\langle\omega_c\tau\rangle\rangle\sim1$. The inequality in Eq. (A17) is, thus, satisfied over a wide range of frequencies but will fail for some very low value of frequency. Similar arguments regarding ϵ_{32}, wherein the sum involving ω is important, lead to

$$-i\epsilon_{32}/\epsilon_{33}\cong(k_\perp\bar{V}/\langle\langle\omega_c'\rangle\rangle)\ll1, \quad \text{(A18)}$$

where $\langle\langle\omega_c'\rangle\rangle$ expresses another suitable average.

The wave equation in electric field $\mathbf{E}$,

$$\mathbf{k}\times(\mathbf{k}\times\mathbf{E})+k_0^2\boldsymbol{\epsilon}\cdot\mathbf{E}=0, \quad \text{(A19)}$$

yields, for the dielectric tensor $\boldsymbol{\epsilon}$ with elements as discussed above, the secular equation

$$\begin{vmatrix} -k_z^2+k_0^2\epsilon_\perp & ik_0^2\epsilon_x & k_\perp k_z-\tan\theta\, k_0^2(\epsilon_\perp-\epsilon_\omega) \\ -ik_0^2\epsilon_x & -k^2+k_0^2\epsilon_\perp & i\tan\theta\, k_0^2\epsilon_x \\ k_\perp k_z+k_0^2\epsilon_{31} & k_0^2\epsilon_{32} & -k_\perp^2+k_0^2\epsilon_{33} \end{vmatrix}=0, \quad \text{(A20)}$$

where $k^2=k_\perp^2+k_z^2$ and $\tan\theta=k_\perp/k_z$. Expansion (the bottom row is most convenient) and division by ϵ_{33} yields

$$(1-\tan\theta\,\epsilon_{31}/\epsilon_{33})K+(k_\perp^2+\tan\theta\, k_0^2\epsilon_{31})(k^2-k_0^2\epsilon_\perp)\epsilon_\omega/\epsilon_{33} +i[k_\perp^2(1-\tan^2\theta)-k_0^2\epsilon_\omega]\tan\theta\, k_0^2\epsilon_x\epsilon_{32}/\epsilon_{33}=0, \quad \text{(A21)}$$

where

$$K\equiv(k_z^2-k_0^2\epsilon_\perp)(k^2-k_0^2\epsilon_\perp)-k_0^4\epsilon_x^2. \quad \text{(A22)}$$

By Eq. (A17), the factor multiplying K in Eq. (A21) becomes unity. By Eq. (A18), and since, by Eq. (A10),

$\tan\theta\, k_0^2\epsilon_x = -k_\perp j/H$, the last term of Eq. (A21) is much smaller in magnitude than the terms in K. Finally, the factor $(k_\perp^2+\tan\theta\, k_0^2\epsilon_{31})$ is by Eqs. (A17) and (A14) approximately $k_\perp^2(1+i\bar{V}^2 en/\langle\langle\omega_c\rangle\rangle)$. The small imaginary term is neglected because even the real part is able to make only a small correction. Thus, Eq. (A21) becomes

$$K-k_\perp^2(k^2-k_0^2\epsilon_\perp)\epsilon_\omega/\epsilon_{33}=0. \quad \text{(A23)}$$

Before obtaining the final form of the dispersion relation, it is instructive to compare it in the form of Eq. (A23) with the normal result obtained when $j=0$. In that case, all off-diagonal elements of $\boldsymbol{\epsilon}$ would vanish unless one were to retain the helicon term. The latter would require $\epsilon_{12}=-\epsilon_{21}=i\epsilon_0\equiv\omega e\delta n/H_z$, which stems from the first term in Eq. (A9). In addition, the diagonal elements $\epsilon_\perp$ would reduce to ϵ_ω unless the Alfvén wave terms ϵ_A were retained as an additional contribution. The equivalent of Eq. (A23) is then the exact result

$$K'+k_\perp^2[(k^2-k_0^2\epsilon_A-k_0^2\epsilon_\omega)\times(\epsilon_A+\epsilon_\omega)+k_0^4\epsilon_\delta^2]/\epsilon_{33}=0, \quad \text{(A24)}$$

where

$$K'\equiv(k_z^2-k_0^2\epsilon_A-k_0^2\epsilon_\omega)\times(k^2-k_0^2\epsilon_A-k_0^2\epsilon_\omega)-k_0^4\epsilon_\delta^2. \quad \text{(A25)}$$

The nature of the waveguide cutoff of the various waves is determined basically by the condition $K'=0$. It shows a "fast" Alfvén wave with cutoff $(k^2=k_0^2\epsilon_A)$ and a "slow" one without cutoff $(k_z^2=k_0^2\epsilon_A)$ and a helicon $(kk_z=\pm k_0^2\epsilon_\delta)$ without cutoff. The waves which are the subject of this paper stem from $K=0$ and have a cutoff $(kk_z=\pm k_0^2\epsilon_x$ or $k\equiv(k_z^2+k_\perp^2)^{1/2}=\pm j/H_z)$.

The present discussion of a comparison of Eqs. (A23) and (A24) centers around the additional term in these equations proportional to $k_\perp^2$, which becomes important when the k's in $K(K')$ become of order $k_\perp$, as near cutoff. The correction is of particular importance when $\omega_c\tau$ is small, since ϵ_{33} is then small also. Comparison of Eqs. (A23) and (A24) shows that plasma compensation $(\epsilon_\delta=0)$ and neglect of ϵ_A are responsible for the simpler form of Eq. (A23), and that (after the approximations listed above) the influence of j enters the $k_\perp^2$ term only through $\epsilon_\perp$. The one important conclusion derived from this discussion concerns the difference in the $k_\perp^2$ correction term at low $\omega_c\tau$ for helicons and the j-dependent waves. Though both are circularly polarized and both stem from the ϵ_{12} element, the plasma compensation in the latter case removes the largest contribution $k_0^4\epsilon_\delta^2$ to the $k_\perp^2$ expression. It is, therefore, possible to retain the simple expression $K=0$ closer to waveguide cutoff with small $\omega_c\tau$ in this case than in the case of helicons.

The final form of Eq. (A23) results from substitution of Eqs. (A16) and (A22), from which

$$k^2k_z^2-2kk_z\gamma k_0^2\epsilon_\perp-k_0^4(\epsilon_x^2-\epsilon_\perp^2)/(1+\Theta)=0, \quad \text{(A26)}$$

where

$$\Theta=\tan^2\theta/(\langle\langle\omega_c\tau\rangle\langle\langle\omega_c\tau\rangle\rangle), \quad \text{(A27)}$$

$$2\gamma=\cos\theta+(1-\Theta)/\cos\theta. \quad \text{(A28)}$$

The $k_\perp^2$ term discussed above results in the $\Theta\neq0$ contribution. In case $\epsilon_x^2\gg\epsilon_\perp^2$ and Θ small, as in our experimental situation just above waveguide cutoff,

$$kk_z=\pm k_0^2\epsilon_x/(1+\Theta)+\gamma k_0^2\epsilon_\perp. \quad \text{(A29)}$$

Substitution of Eqs. (A8) and (A10) gives

$$kk_z=\pm\frac{\cos\theta\, kj}{H_z(1+\Theta)}+i\gamma\frac{\omega en-\Delta\cos\theta\, kj}{H_z\langle\omega_c\tau\rangle}, \quad \text{(A30)}$$

or

$$k^2=\pm\frac{kj}{H_z(1+\Theta)}+\frac{i\gamma}{\cos\theta}\frac{\omega en-\Delta\cos\theta\, kj}{H_z\langle\omega_c\tau\rangle}. \quad \text{(A31)}$$

Equation (A31), for $\Theta=0$, is precisely the expression used in deriving Eq. (2) of Ref. 1.

APPENDIX B: RELATION BETWEEN MATERIAL PARAMETERS AND $\omega_{\max}$

It was established in Sec. II that the waveguide cutoff condition $j>j_c\equiv k_\perp H$ is a necessary condition for wave propagation, although for large frequencies it may not be sufficient for gain. It is a curious property of the system under study that the condition $j>k_\perp H$ involves in no direct way the parameters of the material of which the waveguide is made. It involves only externally applied parameters and dimensions. We may well ask, then, what determines the choice of material and the corresponding upper cutoff frequency for gain. We may also ask how universally applicable this condition will be to such related systems as the negative-energy (NE) mode in partially compensated plasmas[2] and layered plasma structures.[12]

The choice of material for the waveguide comes down to the practical limitation of how much power can be dissipated in the case of continuous operation. We assume here that the material has properties, such as anisotropic mobilities, suitable for producing gain. The power generated per unit length of circular waveguide operating at $j=2j_c$, P_L, is given by the power density times the cross-sectional area

$$P_L\equiv\pi r^2j^2/\sigma=4(2.405)^2\pi H^2/\sigma, \quad \text{(B1)}$$

where σ is the conductivity and $j=2j_c$ is substituted from Eqs. (9) and (10), neglecting terms in Θ. Since P_L is independent of radius, the power flowing out per unit area of waveguide circumference, P_A, increases with a decrease of waveguide diameter;

$$P_A=2(2.405)^2H^2/r\sigma. \quad \text{(B2)}$$

In waveguides with a specific radius, operation with gain at a certain high frequency may require a current

[12] G. A. Baraff, J. Phys. Chem. Solids **28**, 1037 (1967).

density greater [given by Eq. (16)] than $j=2j_c$. If j is increased to get gain, the radius must be reduced in order to avoid the absolute instability mode of self oscillation. From Eqs. (8) and (16) and $j=2j_c$,

$$\omega_{\max}\equiv(3\Delta H/en)(2.405/r)^2, \tag{B3}$$

where n is the total concentration of electrons plus holes and $\Theta=0$. The power per unit surface area will increase as $\omega_{\max}$ is raised through a reduction of r. Eliminating r between Eqs. (B2) and (B3), we find that

$$\omega_{\max}=\tfrac{3}{4}\Delta[\mu\sigma/(2.405)^2H^3]P_A^2, \tag{B4}$$

where $\mu\equiv\sigma/ne$ is the net mobility of all the carriers. In Eq. (B4), $\omega_{\max}$ is expressed in terms of the fundamental parameters of the material and the practical limit imposed by the heat sink's ability to conduct away the heat generated. Thermal conductivity limitations of the waveguide material have been neglected.

The significance of Eq. (B4) in determining the best choice of material is the followlng. $\omega_{\max}$ varies as H^{-3}, so that the lowest field is the best (neglecting the possible limit imposed by the requirement $\omega\ll\omega_c$). This field is qualitatively given by $\omega_c\tau\sim1$, so that $H\propto1/\mu_C$. The net effect is then that

$$\omega_{\max}\propto\mu^5nP_A^2. \tag{B5}$$

It would appear that Bi, with the highest available mobility at appreciable values of n, offers the best choice, particularly when coupled with an efficient heat sink.

In the remainder of Appendix B, we show that Eq. (B4) is also applicable to the NE mode of amplification with the exception of a slightly different numerical constant replacing Δ. As described in Ref. 2, the NE mode occurs only in plasmas with unequal electron and hole concentrations characterized by the parameter $\delta n/n(\neq0)$.

It was shown also that if the resistance is positive at the peak point of the NE branch, a resistive absolute instability mode would occur. Avoiding this condition but amplifying to the highest possible frequency, therefore, requires

$$\Delta\delta n/n=\tfrac{1}{2}. \tag{B6}$$

In the simplest case of NE amplification, using carriers with isotropic and equal mobilities, Δ takes the form $\Delta=\delta n/n$. Thus, from Fig. 10 and Eq. (B6),

$$\omega_{\max}=j^2/4He\delta n=(\tfrac{1}{4}\sqrt{2})j^2/Hen. \tag{B7}$$

Equation (B7) compares with Eq. (16), except that waveguide effects have been ignored in Eq. (B7). The waveguide problem for the NE mode is not developed here, although it is well known that helicons do not exhibit a distinct cutoff. The effect giving rise to the NE branch, however, has the same vectoral considerations as those given for the NR mode in Sec. II and Appendix A. If we arbitrarily make use of Eq. (8) (with $\Theta=0$) to replace j^2 in Eq. (B7), we obtain for the case of NE amplification at $\omega_{\max}$ an expression to compare with Eq. (B4);

$$\omega_{\max}=(3\sqrt{2}/16)[\mu\sigma/(2.405)^2H^3]P_A^2. \tag{B8}$$

The difference between the NE and NR modes is, therefore, in the ratio of $(\sqrt{\tfrac{1}{2}})$ (which is 0.35) to Δ, a minor difference, indeed.

The same practical limitation also appears to apply to layered structures[2,3] consisting of adjacent slabs of current-carrying and passive uncompensated plasma. Instability is also caused by a NE helicon wave and will have much the same waveguide cutoff considerations. It is not certain at this time if it is subject to the equivalent of the limitation $(\delta n/n>1/\sqrt{2})$ on frequency imposed by the onset of absolute instability for the NE mode. An appropriate equivalent limitation may be, for example, on the ratio of areas of the current carrying and passive plasma portions within the waveguide. Some such limitation appears to be reasonable.

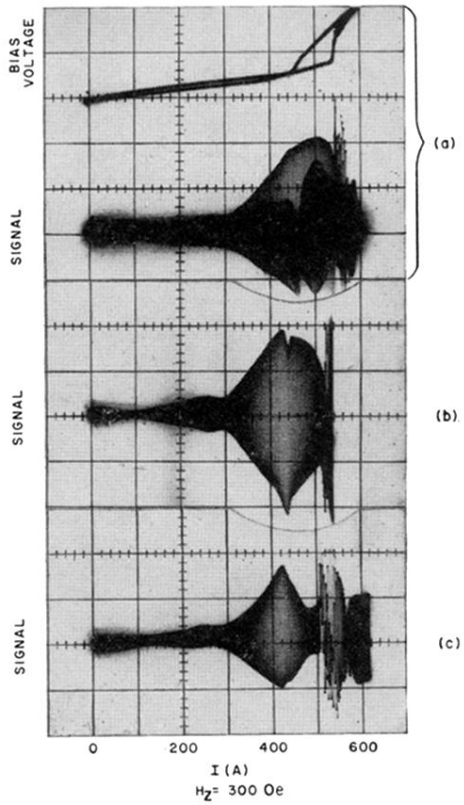

FIG. 10. Same as 7(c) but for sample angle tilted successively, up to 9° in (c). In (a), the return trace is shown superimposed on the outgoing trace. Outgoing trace only is shown in (b) and (c) and Fig. 7.

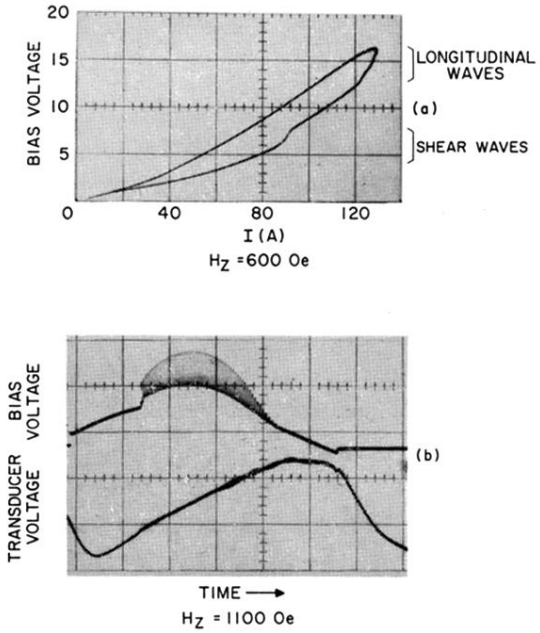

FIG. 11. (a) Current-voltage relation showing voltage steps interpreted as resulting from phonon emission. (b) Upper trace: bias voltage oscillations associated with absolute instability mode. Lower trace: output from low-frequency acoustic transducer showing persistence of oscillation after cessation of current.

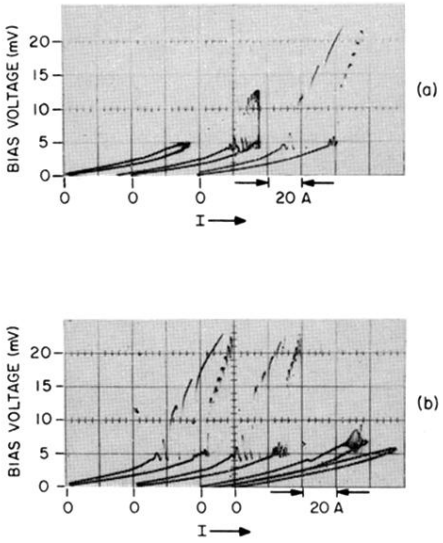

FIG. 12. (a) Development of strongly nonlinear current-voltage relation when maximum current excursion is increased ($H_z = 350$ Oe). (b) As in (a) except that current excursion is constant and H_z has the values 350, 400, 570, and 1100 Oe.

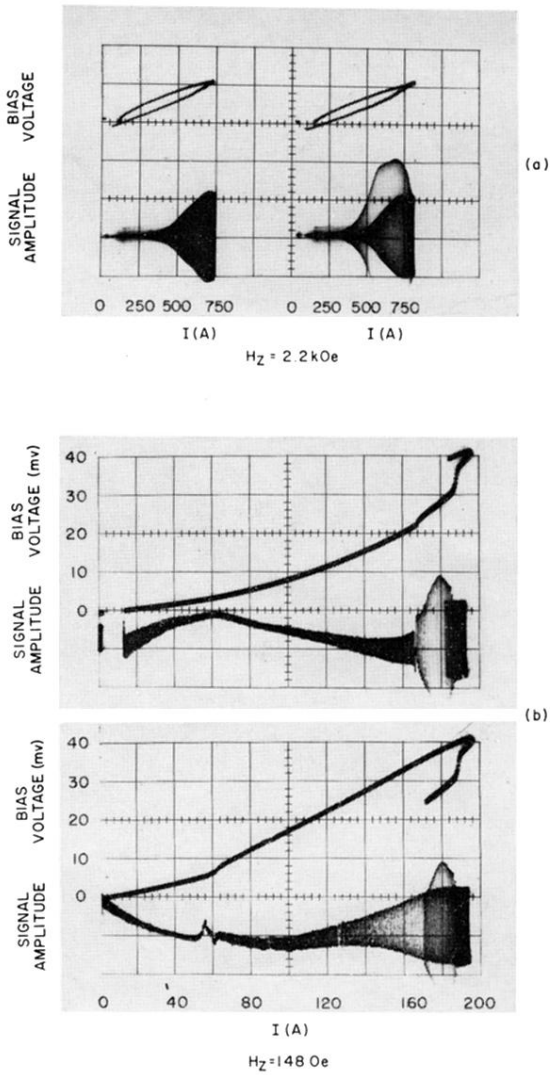

FIG. 13. (a) Bias voltage and transmission response of sample B-21 with $H_z = 2.2$ kOe for two settings of maximum current excursion. (b) Upper and lower figures are outgoing and return traces, respectively, of bias voltage and transmission response of sample B-27 ($I_w = 0$) with $H_z = 148$ Oe.

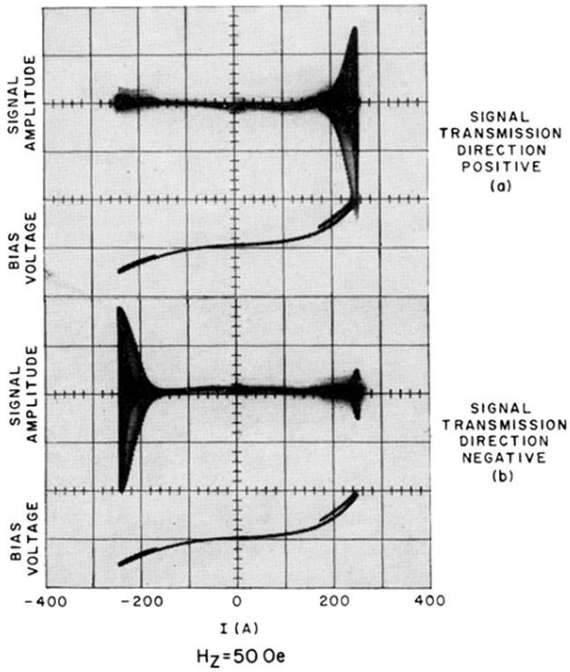

FIG. 14. Signal amplitude and bias voltage of sample B-27 when the signal is transmitted in the two opposite directions, parts (a) and (b).

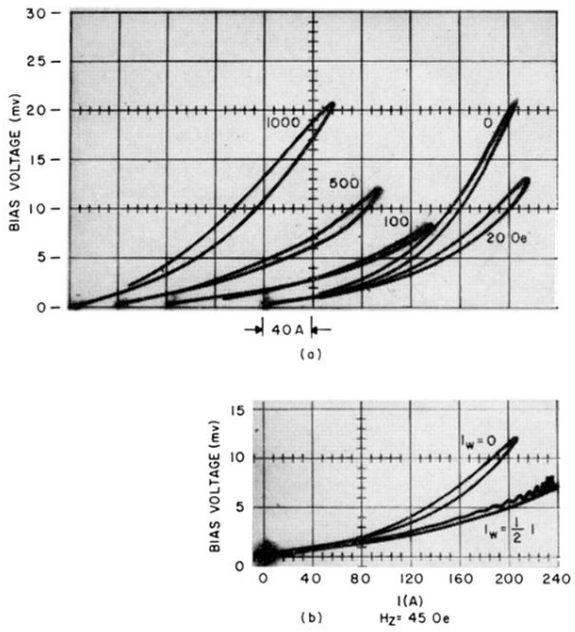

FIG. 15. (a) Bias current-voltage relation of sample B-27 for various fields and $I_w=0$. (b) Same as (a), 45 Oe with $I_w=0$ and $\frac{1}{2}I_s$.

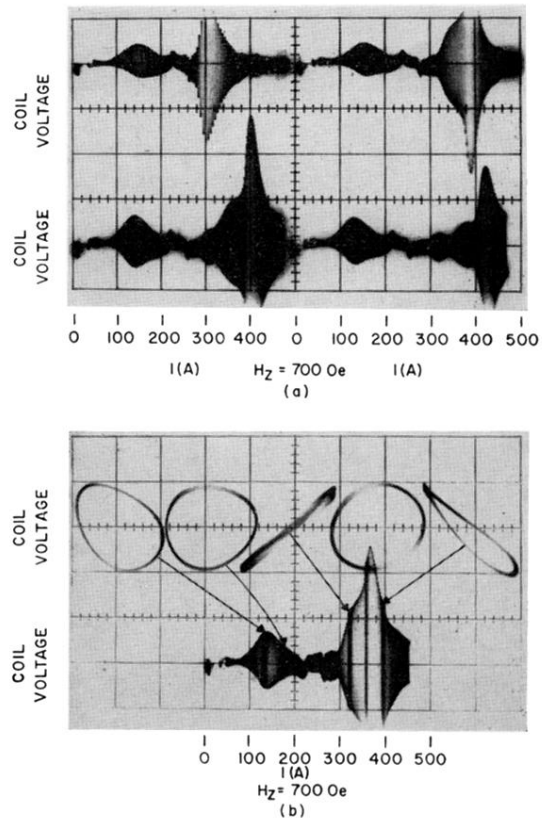

FIG. 16. (a) Coil voltage of sample B-21 at $H_z = 700$ Oe for four frequencies, 25, 50, 75, and 100 kHz. (b) 50-kHz response showing also the phase of the enhanced portions.

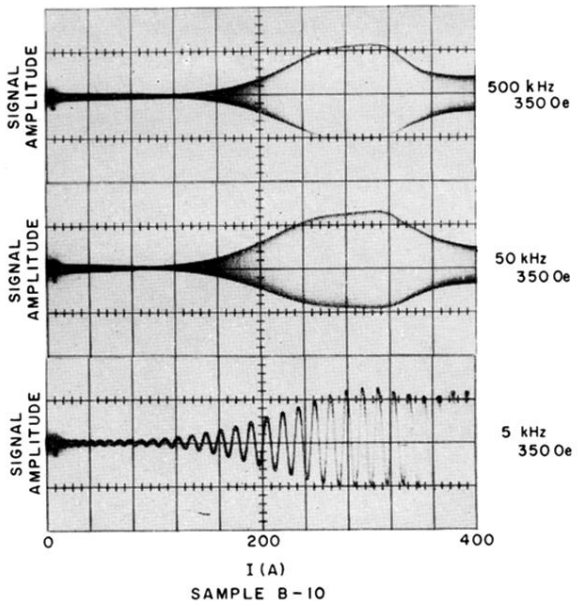

FIG. 5. Response of sample B-10 at three frequencies.

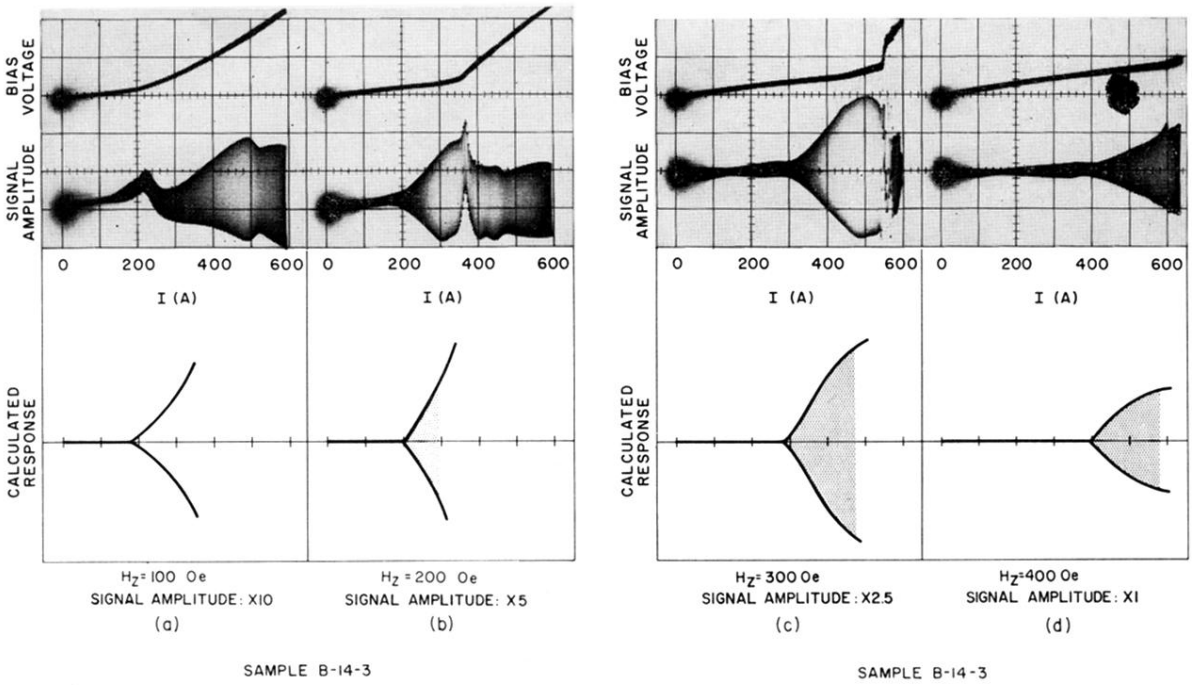

FIG. 7. Bias voltage and observed and calculated amplitude response of sample B-14-3 for 4 values of field, (a)–(d). Note change in relative signal amplitude in parts (a)–(d). Shaded portion of calculated curves indicate region of applicability.

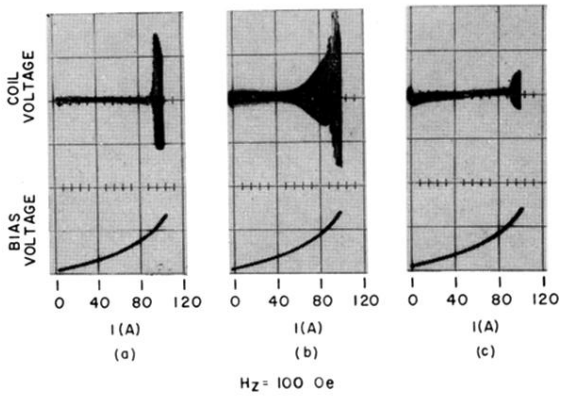

FIG. 8. (a) Self oscillation in sample B-27 with $H_z = 100$ Oe and $I_w = \frac{1}{2}I$. (b) As in (a) but with 30-kHz signal applied. (c) As in (b) but with the transmission direction reversed.

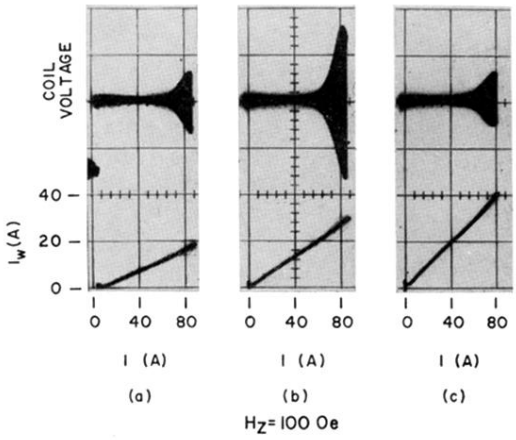

FIG. 9. As in Fig. 8(b) but with various ratios of I_w/I.